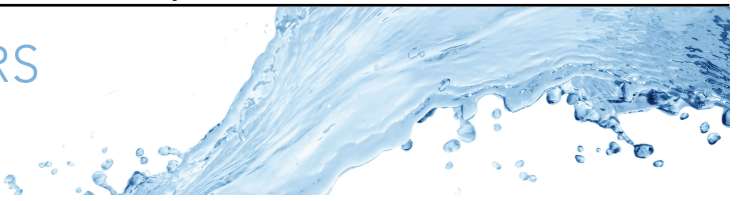
J. Fluid Mech. (2025), *vol.* 1022, A24, doi:10.1017/jfm.2025.10798



Surfactant-laden film lining an oscillating cap: nonlinear dynamics and monolayer collapse

Vasilis Bontozoglou

Department of Mechanical Engineering, University of Thessaly, Volos 38334, Greece

Corresponding author: Vasilis Bontozoglou, bont@mie.uth.gr

(Received 17 June 2025; revised 3 September 2025; accepted 4 October 2025)

A spherical cap, lined internally with a surfactant-laden liquid film, is studied numerically as a model of lung alveoli. Large-amplitude oscillations are considered (deep breathing), which may lead to collapse of the surfactant monolayer during compression, with formation of a sub-surface reservoir that replenishes the monolayer during re-expansion. Independent conservation equations are satisfied for the monolayer and the total surface concentration of surfactant and a novel kinetic expression is introduced to model the two-way internal transport with the reservoir. Marangoni stresses, which drive shearing flow, are not significantly hindered by the collapse of the monolayer, unless the latter is singularly stiff. However, volumetric flow rate and wall shear stress exhibit abrupt changes with monolayer collapse, mainly because of the strong modification of capillary stresses. These changes induce complex temporal variability in the epithelial shear, a condition known to stimulate enhanced surfactant secretion. The effect may counterbalance the predicted increase with amplitude in surfactant drift from the alveolar opening, thereby contributing to homeostasis. Nano-particles deposited on the liquid layer are slowly transported by the flow towards the alveolar rim, with exit half-time in order-of-magnitude agreement with *in vivo* data. Thus, Marangoni stresses are proposed as a key mechanism of alveolar clearance. Both particle displacement speed and surfactant drift from the alveoli are found to vary with solubility, with the former increasing monotonically and the latter exhibiting maximum at intermediate solubilities.

Key words: pulmonary fluid mechanics, lubrication theory, capillary flows

1. Introduction

Interfacial flows with insoluble or soluble surfactants are intensely studied in the recent literature and the presence of the surface-active agent has a decisive role in the stability

© The Author(s), 2025. Published by Cambridge University Press. This is an Open Access article, distributed under the terms of the Creative Commons Attribution licence (https://creativecommons.org/licenses/by/4.0/), which permits unrestricted re-use, distribution and reproduction, provided the original article is properly cited.

https://doi.org/10.1017/jfm.2025.10798 Published online by Cambridge University Press

characteristics and transitions, as well as in accompanying transport phenomena (Frenkel & Halpern 2002; Blyth & Pozrikidis 2004; Pereira *et al.* 2007; Craster & Matar 2009; Kalogirou & Papageorgiou 2015; Manikantan & Squires 2020; Hu, Fu & Yang 2020; Constante-Amores *et al.* 2021; D'Alessio & Pascal 2021; Samanta 2021; Miguet, Dorbolo & Scheid 2024; Samanta 2025). The dynamics of such flows is frequently dictated by the coupling of the flow field with the characteristics of the surfactant monolayer, for example its surface elasticity and viscosity, and with the kinetics of surfactant exchange between the surface and the bulk. This coupling becomes more involved when the monolayer is dense, or even close to collapse, in which case its dynamics cannot be described by simple linear relations.

A relevant application, of particular interest to mammalian physiology, is the behaviour of the surfactant-laden liquid layer that lines internally the lung airways and alveoli (Gaver & Grotberg 1990; Halpern, Jensen & Grotberg 1998; Matar, Zhang & Craster 2003; Grotberg 2011; Kim *et al.* 2011; Filoche, Tai & Grotberg 2015; Muradoglu *et al.* 2019; Bouchoris & Bontozoglou 2022; Romanò *et al.* 2022). In the case of alveoli, this layer consists of an aqueous phase, with estimated thickness $0.1-1\,\mu\mathrm{m}$ depending on lung inflation and health condition (Bastacky *et al.* 1995; Wei *et al.* 2005). Its interface with the air is covered by a monolayer of pulmonary surfactant, a mixture of lipids (mainly dipalmitoylphosphatidylcholine (DPPC)) and proteins (SP-A, SP-B, SP-C Zuo *et al.* (2008)). These molecules are sparingly soluble, so any excess resides inside the liquid film in the form of micelles (Perez-Gil 2008). The key property of the surfactant monolayer is its ability to reduce drastically surface tension at the interface, thus making the alveoli more compliant and reducing the metabolic work of breathing (Zasadzinski *et al.* 2001; Rugonyi, Biswas & Hall 2008; Zhang *et al.* 2011).

The hydrodynamics of the liquid layer lining the alveoli has been repeatedly a topic of investigation during recent decades (Gradon & Podgorski 1989; Podgorski & Gradon 1993; Espinosa & Kamm 1997; Zelig & Haber 2002; Wei *et al.* 2003, 2005; Halpern *et al.* 2008; Kang *et al.* 2018; Bouchoris & Bontozoglou 2022). The reason for this interest is that slow shearing motions (i.e. velocities parallel to the alveolar epithelium), which may develop triggered by the radial oscillation of the alveolar wall, are potentially of importance for lung homeostasis, for example in cell–cell signalling and in cleansing the alveolus from deposited particles. Two key mechanisms that may create a shearing motion are Marangoni (elastic) stresses that result from spatial variation of surface tension and capillary stresses that result from spatial variation of the interfacial curvature.

Bouchoris & Bontozoglou (2022) modelled alveoli as spherical caps in self-similar oscillations and argued that the boundary conditions imposed at the rim are critical for correct modelling of the flow field in the liquid lining. A novel boundary condition was implemented by these authors, which takes into account the small but finite thickness of the mid-alveolar septum and avoids the imposition of pre-specified values of film thickness and surfactant concentration at the rim. This approach appears to provide realistic estimates for key variables, such as the shear stress imposed along the epithelium, and also offers interesting predictions for conditions in a diseased lung (Livanos *et al.* 2024).

However, the study by Bouchoris & Bontozoglou (2022) is limited to linear and weakly nonlinear oscillations of the alveolar wall around its equilibrium position, i.e. formally to alveolar radius variations of order $\pm 1\,\%$. Thus, the following questions naturally arise: (i) Is linear theory sufficient for the description of smooth breathing, where radius oscillations are typically around $3\,\%-5\,\%$? (ii) Are there any significant nonlinear phenomena in this breathing regime? (iii) What is the flow field in the liquid layer during deep breathing,

https://doi.org/10.1017/jfm.2025.10798 Published online by Cambridge University Press

where the alveolar radius may vary by 10 %−20 %? The investigation of such questions necessitates solution of the full nonlinear problem, which is the goal of the present work.

The pulmonary surfactant monolayer is known to undergo significant structural changes with the occurrence of large variations in its surface area. These changes have been extensively investigated in the relevant literature and many illuminating reviews are available (Possmayer *et al.* 2001; Zasadzinski *et al.* 2001; Wüstneck *et al.* 2005; Lee 2008). In particular, the monolayer may sustain large compressions during contraction, eventually reducing its surface tension to values below 0.005 N m^{-1}, while changing its structure to a liquid expanded phase and then to a tilted condensed phase (Crane, Putz & Hall 1999; Yan, Piknova & Hall 2005; Zuo *et al.* 2008; Zhang *et al.* 2011; Parra & Perez-Gil 2015).

Further compression results in collapse of the surfactant monolayer and formation of a reservoir sublayer (Krueger & Gaver 2000). The onset of collapse is characterised by a minimum value of the surface tension, σ_{min}, and a maximum value of the surface concentration of surfactant, Γ_{max}, both of which remain constant until the end of the contraction stage. The reservoir sublayer appears to form by buckling and folding events, giving rise to protrusions that extend away from the monolayer and towards the interior of the liquid while remaining connected to the monolayer (Lipp *et al.* 1998; Schief *et al.* 2003; Baoukina *et al.* 2008; Lee 2008; Saad, Neumann & Acosta 2010; Phan, Lee & Shin 2016; Xu, Yang & Zuo 2020). The connection of the reservoir to the monolayer is very important because it allows rapid replenishment of the monolayer content during expansion, thus restricting the rise in surface tension (Wüstneck *et al.* 2001; Parra & Perez-Gil 2015).

In the present work, the evolution equations for the liquid film thickness, h, and the surface surfactant concentration, Γ, of an internally lined oscillating spherical cap – derived by Bouchoris & Bontozoglou (2022) using a lubrication approximation in the Stokes limit – are supplemented by an evolution equation for the pure monolayer concentration, Γ_m. Thus, capillary and Marangoni stresses, which actually vary with the monolayer and not the total surface concentration, are correctly described for large-amplitude oscillations that result in monolayer collapse.

A novel kinetic expression is introduced, which models the replenishment of the monolayer by surfactant from the reservoir, $(\Gamma - \Gamma_m)$, during re-expansion of the alveolus. Even more important, the kinetic expression includes a term that restricts monolayer concentration to values $\Gamma_m \leqslant \Gamma_{max}$, while introducing a parameter, k_{rc}, that quantifies the abruptness of monolayer collapse. The resulting system of nonlinear equations is spatially discretised by a Galerkin finite-element method and solved by a Newton–Raphson iterative scheme, with the time derivatives treated fully implicitly.

The paper is organised as follows. The problem set-up in § 2 includes formulation of the dynamics of the liquid layer, the dynamics and the mass balances of the surfactant and the boundary and initial conditions. In § 3, the equations are scaled using equilibrium variables and their numerical solution is outlined. Section 4 contains results for the dynamics of large-amplitude oscillations (without and with monolayer collapse) and investigates in particular the displacement of insoluble particles (passive tracers) deposited on the liquid layer and the drift of surfactant from the alveolar opening. Finally, conclusions are drawn in § 5.

2. Problem set-up

2.1. *Outline of the modelling procedure*

Model development necessitates combined consideration of (i) the fluid dynamics of the liquid layer, (ii) the mass exchange dynamics at the interface and (iii) the conservation

https://doi.org/10.1017/jfm.2025.10798 Published online by Cambridge University Press

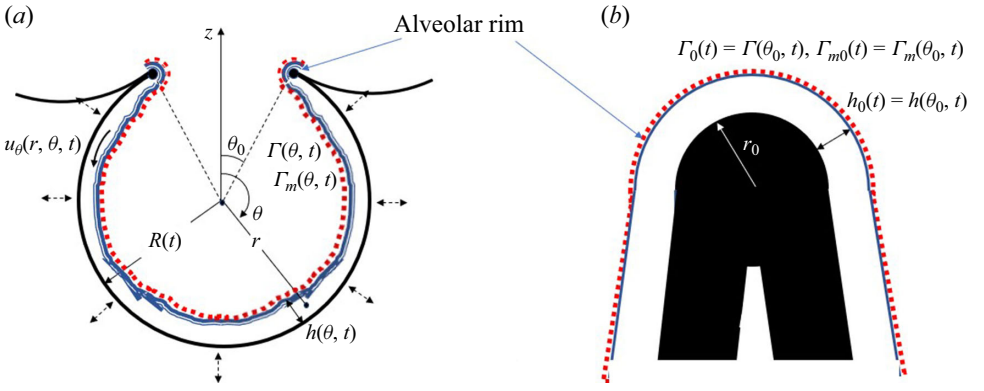


Figure 1. (*a*) A sketch of the spherical cap with the main problem parameters and (*b*) magnification of the rim with the local parameter values (red colour marks the hydrophobic end of surfactant molecules).

equations of surfactant. The derivations, although not particularly difficult, are involved and with rather numerous intermediate steps, so the following outline may be helpful.

The fluid dynamics of the liquid layer is described by the Navier–Stokes equation in the low Reynolds number limit, with free-surface boundary conditions applied along the interface. The dynamic boundary condition contains the local values of surface tension (in the capillary stress term) and its spatial gradients (in the Marangoni stress term). The surface tension is considered a sole function of the local monolayer concentration, Γ_m, and thus its values – as well as those of surface elasticity – are derived from an equation of state that follows from Gibbs' theory, with key novelty the inclusion of the intrinsic compressibility of the adsorbed monolayer.

Surfactant concentration on the interface is described by two terms, Γ_m, which gives the surface concentration of the adsorbed monolayer and Γ, which, includes both the monolayer surfactant and the surfactant contained in the sublayer reservoir that forms during monolayer collapse. Two conservation equations are thus formulated to follow the spatio-temporal evolution of the above surface concentrations, which include the contributions of interfacial expansion/contraction, of convection and diffusion along the interface and of mass exchange with the environment.

The mass exchange terms are crucial inputs to the surfactant conservation equations, and they consist of the following two contributions. The flux j_b, which describes adsorption/desorption between the monolayer and the bulk, and is modelled by Langmuir kinetics in terms of an adsorption rate and an equilibrium constant. The flux, j_r, which describes internal exchange between the monolayer and the reservoir, and is modelled by a Langmuir-like term that accounts for monolayer replenishment from the reservoir during interface expansion and by a singular term that limits maximum monolayer concentration below Γ_{max} during interface contraction. In the following paragraphs, each of the aforementioned dynamic components of the model is considered in detail.

2.2. *Dynamics of the liquid layer*

The alveolus is modelled as a spherical cap with an opening angle $2\theta_0$ ($\theta_0 = 30°$ for a normal alveolus), as shown in figure 1(*a*). During oscillation, the opening angle remains constant, i.e. the alveolus retains a self-similar shape (Tsuda, Henry & Butler 2008). Although there are alternative choices for the exact alveolar shape, the truncated sphere remains the most common model geometry in the literature (Kolanjiyil & Kleinstreuer 2019). The alveolar rim is taken to have a semicircular cross-section of small but finite

https://doi.org/10.1017/jfm.2025.10798 Published online by Cambridge University Press

radius r_0 (figure 1*b*). Thus, the local septal thickness is $\sim 2r_0$. Due to the finite thickness, water and surfactant accumulate on the rim and local values of film thickness and surfactant concentration, which continuously vary during alveolar oscillations, enter the boundary conditions (Bouchoris & Bontozoglou 2022).

The liquid layer is Newtonian (Grotberg 2011), with density ρ and viscosity μ. The flow is taken to be symmetric in the circumferential direction and is analysed in a spherical coordinate system (r, θ, ϕ) located at the centre of the cap. Thus, the flow field is described by the velocity vector $\boldsymbol{u} = (u_r(r, \theta, t), u_\theta(r, \theta, t), 0)$ and the pressure distribution $p(r, \theta, t)$. The air–liquid interface is located at $r = R(t) - h(\theta, t)$, where $h(\theta, t)$ is the liquid film thickness. It is further characterised by its surface tension, $\sigma(\theta, t)$, which varies in space and time as it is determined by the local concentration of the surfactant monolayer.

Following standard practice in the literature (Podgorski & Gradon 1993; Haber *et al.* 2000; Zelig & Haber 2002; Wei *et al.* 2005; Kang *et al.* 2018), the flow is described by the continuity and the quasi-steady Stokes equation, subject to the no-slip boundary condition on the wall and the kinematic and dynamic boundary conditions along the interface. The dynamic condition includes components normal and tangential to the interface, the former proportional to surface tension and local curvature (capillary stress) and the latter proportional to the local spatial gradient of surface tension (Marangoni stress). The equations are further simplified by a lubrication assumption, which is based on the large scale difference between the r- and θ-directions ($h << R$). The final result is the following evolution equation that describes the spatio-temporal variation of the liquid film thickness, driven by capillary and Marangoni stresses (respectively, the first and second terms in the parenthesis). The details of the mathematical derivation are presented in a previous paper (Bouchoris & Bontozoglou 2022) and are also discussed by Kang *et al.* (2018)

$$\frac{\partial h}{\partial t} + \frac{2h\dot{R}}{R} - \frac{1}{R^2 \sin\theta}\frac{\partial}{\partial \theta}\left(\frac{h^3 \sin\theta}{3\mu}\frac{\partial p}{\partial \theta} - \frac{h^2 \sin\theta}{2\mu}\frac{\partial \sigma}{\partial \theta}\right) = 0. \tag{2.1}$$

It is noted that, in the lubrication approximation, pressure is uniform in the radial direction and can be described by the following expression, using the normal boundary condition on the interface:

$$p(\theta, t) = p_{air} - \sigma\left[\frac{2}{R} + \frac{2\,h}{R^2} + \frac{1}{R^2 \sin\theta}\frac{\partial}{\partial \theta}\left(\sin\theta\,\frac{\partial h}{\partial \theta}\right)\right]. \tag{2.2}$$

The term in parenthesis in (2.1) is equal to $-Q(\theta, t)/2\pi$, where

$$Q(\theta, t) = 2\pi R\,\sin\theta \int_{R-h}^{R} u_\theta\,\mathrm{d}r = 2\pi\,\sin\theta\left(-\frac{h^3}{3\mu}\frac{\partial p}{\partial \theta} + \frac{h^2}{2\mu}\frac{\partial \sigma}{\partial \theta}\right), \tag{2.3}$$

is, in the lubrication limit, the volumetric flow rate along the entire ϕ-circumference. Thus, (2.1) may be rewritten as

$$\frac{\partial}{\partial t}\left(2\pi R^2 \sin\theta\, h\right) + \frac{\partial Q}{\partial \theta} = 0, \tag{2.4}$$

which is intuitively more evident as the mass balance of liquid in a differential control volume along the entire ϕ-periphery at the location θ.

The derivations leading to (2.1) – as well as the entire paper – neglect the effect of the dynamics of airflow inside the alveolus during the breathing cycle. The following simple scaling argument, based on the continuity of shear stress and velocity at the air–liquid interface, shows that the effect is indeed negligible. More specifically, if $u_{s,a}$ is the liquid

https://doi.org/10.1017/jfm.2025.10798 Published online by Cambridge University Press

interfacial velocity tentatively imposed by gas shear

$$\mu_a \left(\frac{\partial u}{\partial y}\right)_a \sim \mu \frac{\partial u}{\partial y} \Rightarrow \mu_\alpha \frac{u_a - u_{s,a}}{\bar{R}} \sim \mu \frac{u_{s,a} - 0}{\bar{H}} \Rightarrow u_{s,a} \sim u_a \frac{\mu_a}{\mu} \frac{\bar{H}}{\bar{R}}. \tag{2.5}$$

Given that $\mu_a/\mu \sim 1:50$ and $\bar{H}/\bar{R} \sim 0.3:100$, the liquid velocity imposed by air shear is four orders of magnitude smaller than the typical air velocity inside the alveolus, i.e. two to three orders of magnitude smaller than the shearing velocity on the liquid film triggered by Marangoni stresses (as shown by Bouchoris & Bontozoglou (2022), the shearing velocity is one to two orders of magnitude smaller than the radial velocity of the alveolar wall).

An assumption, implicit in the above formulation, is the neglect of the potential role of surfactant aggregates in the liquid film dynamics. The dynamics of the aggregates themselves is probably related to the kinematics of surfactant exchange with the interface and is not in direct interest to the present study. However, given the relative sizes of the aggregates ($\sim$100 μm) and the liquid film ($\sim$200−1000 μm), it is reasonable to expect that, with increasing number density, the aggregates will have a non-negligible effect on the liquid dynamics. Possibilities for including this effect in more refined simulations are mentioned in the Concluding Remarks.

2.3. *Dynamics of the surfactant*

The pulmonary surfactant is a mixture of lipids and proteins, which are practically insoluble in water. It is indicative that the critical micelle concentration (CMC) of the major phospholipids (i.e. the maximum concentration of monomer beyond which monomers combine to form micelles) is $10^{-9}-10^{-10}$ M (Marsh & King 1986). As a result, a portion of the surfactant populates the interface with local surface concentration $\Gamma(\theta, t)$, while the excess amount resides in the bulk in the form of aggregates (Zuo *et al.* 2008; Bykov *et al.* 2021). There is ample experimental evidence (Baoukina & Tieleman 2011; Parra & Perez-Gil 2015; Bouchoris & Bontozoglou 2021) indicating that the adsorption/desorption of surfactant to/from the interface occurs through its direct interaction with these aggregates. The pulmonary surfactant mixture is currently modelled by a single generic surfactant, which mimics the dynamic behaviour of the actual preparation (Wüstneck *et al.* 2005).

The description of the interfacial surfactant composition becomes more involved when the alveolar oscillations are strong enough to include the stages of monolayer collapse and subsequent replenishment. The surface concentration, Γ, now consists of the sum of the monolayer and reservoir concentrations, $\Gamma = \Gamma_m + \Gamma_r$. During compression, the monolayer concentration does not increase beyond the maximum value that corresponds to the minimum attainable surface tension. Thus, $\Gamma_m \to \Gamma_{max}$, where $\sigma(\Gamma_{max}) = \sigma_{min}$, and any further increase of Γ results in an equal increase of Γ_r. It is important to re-iterate that, capillary and Marangoni stresses vary with Γ_m and not with Γ. Figure 2 provides a sketch of the interfacial region and the surfactant exchange processes during compression (figure 2*a*) and during expansion (figure 2*b*).

The local value of surface tension, σ, along the interface is a function of the local monolayer concentration, i.e. $\sigma = \sigma(\Gamma_m)$, and is described by the equation of state to be developed shortly. Considering a space coordinate, s, along the interface, the variation of surface tension and monolayer concentration are related by the chain rule, i.e. $\partial\sigma/\partial s = (\mathrm{d}\sigma/\mathrm{d}\Gamma_m)(\partial\Gamma_m/\partial s)$. The sensitivity of σ to Γ_m is expressed by the Gibbs elasticity, E, where

$$E = -\frac{\mathrm{d}\sigma}{\mathrm{d}\ln\Gamma_m} = -\Gamma_m \frac{\mathrm{d}\sigma}{\mathrm{d}\Gamma_m}. \tag{2.6}$$

https://doi.org/10.1017/jfm.2025.10798 Published online by Cambridge University Press

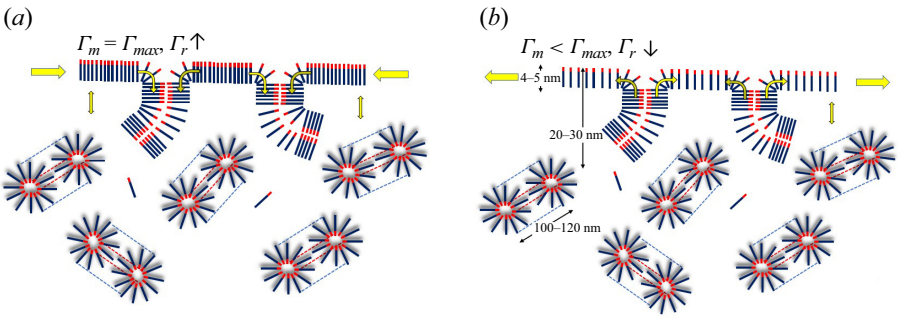


Figure 2. Schematic of the interface with the monolayer and the reservoir protrusions, and the bulk with surfactant aggregates. (*a*) Compression that leads to monolayer collapse and growth of the reservoir. (*b*) Re-expansion, when the monolayer concentration falls below Γ_{max} and is replenished by surfactant from the reservoir. Red colour marks the hydrophobic end of surfactant molecules and bars in (*b*) (not to scale) indicate the sizes of the monomer, the surface layer and the aggregates as measured by Xu *et al.* (2020).

A novel feature of the surfactant model is the inclusion of an intrinsic compressibility, α, of the adsorbed monolayer, as defined and justified by Fainerman, Miller & Kovalchuk (2002) and Kovalchuk *et al.* (2004, 2005). More specifically, the molar surface area of the monolayer, Ω, is taken to vary linearly with surface pressure, $\Pi = \sigma_0 - \sigma$, according to the relation

$$\Omega = \Omega_0(1 - \alpha\Pi), \tag{2.7}$$

where σ_0 is the surface tension of pure water and Ω_0 is the molar area at zero surface pressure. This correction is particularly significant for dense monolayers and was recently shown to offer quantitative agreement of the model dynamics with laboratory measurements using actual pulmonary preparations (Saad *et al.* 2010; Xu *et al.* 2020).

In terms of Ω, the monolayer coverage, γ, is $\gamma = \Gamma_m\Omega$, and thus the surface concentration at interfacial saturation, $\Gamma_{m,\infty}$ (which corresponds to $\gamma = 1$), varies with surface pressure, and is given by

$$\Gamma_{m,\infty} = \frac{1}{\Omega} = \frac{1}{\Omega_0(1 - \alpha\Pi)}. \tag{2.8}$$

Using Gibbs' theory, which is valid for a Gibbs dividing surface and an ideal bulk phase, the following equation of state is derived (Kovalchuk *et al.* 2004), connecting surface pressure to interfacial coverage:

$$\frac{\Pi\Omega_0}{\mathcal{R}\mathcal{T}}\left(1 - \alpha\frac{\Pi}{2}\right) = -\ln(1 - \gamma), \tag{2.9}$$

where $\mathcal{R}$ is the universal gas constant and $\mathcal{T}$ the absolute temperature.

The surface concentration of surfactant varies continuously during breathing as a result of the periodic expansion and contraction of the interface. The variation of Γ_m from the equilibrium value, Γ_{eq} (corresponding to a non-oscillating alveolus for which $\Gamma_{eq} \equiv \Gamma_{m,eq}$) causes a mass flux, j_b, of surfactant between the monolayer and the bulk. Assuming a Langmuir adsorption isotherm, equilibrium is given by the expression

$$KC_{10} = \frac{\Gamma_{eq}}{\Gamma_{eq,\infty} - \Gamma_{eq}}, \tag{2.10}$$

where $\Gamma_{eq,\infty}$ is the saturation value at equilibrium conditions, K is the equilibrium constant and C_{10} the CMC of the monomer in the bulk. Thus, mass exchange with the

https://doi.org/10.1017/jfm.2025.10798 Published online by Cambridge University Press

bulk is expressed as follows in terms of an adsorption rate, k_{ads}:

$$j_b = k_{ads} C_{10} \left[(\Gamma_{m,\infty} - \Gamma_m) - \frac{\Gamma_m}{K\, C_{10}} \right], \tag{2.11}$$

while for an insoluble surfactant $j_b = 0$. It is noted that the above expression for mass exchange is based on kinetic resistance at the interface (rather than diffusion in the bulk), an assumption strongly supported by the literature (Ingenito *et al.* 1999; Saad *et al.* 2010).

Mass exchange between the monolayer and the reservoir, j_r, changes direction during the breathing cycle, because the reservoir stores surfactant during compression (so that Γ_m does not exceed Γ_{max}) and releases it back to the monolayer during re-expansion of the alveolus (when Γ_m falls below Γ_{max}). This dual role is described by the following expression:

$$j_r = k_r (\Gamma_{m,\infty} - \Gamma_m)\, (\Gamma - \Gamma_m) - \frac{k_{rc}}{(\Gamma_{max} - \Gamma_m)^2}. \tag{2.12}$$

The first term in (2.12) gives the rate of replenishment of the monolayer during expansion and is proportional to the potential for replenishment, $(\Gamma_{m,\infty} - \Gamma_m)$, and to the available surfactant concentration in the local reservoir, $(\Gamma - \Gamma_m)$. The second term limits the monolayer concentration to be below the maximum value Γ_{max} during compression. Parameter k_{rc} may be viewed as a measure of the stiffness of the dense monolayer, in the sense that the smaller k_{rc} the closer the monolayer concentration is to its limiting value without collapsing and the more abrupt the collapse. By choosing a very small value $k_{rc} = 10^{-5}$, the contribution of the second term in (2.12) becomes significant only when Γ_m approaches close enough to Γ_{max}.

2.4. *Mass balances of surfactant*

The aforementioned variables, Γ and Γ_m, are functions of location and time, and their evolution is determined by appropriate mass conservation equations. Such equations must include convection and diffusion along the interface and mass exchange with the bulk and the reservoir, and must also take into account the effect of expansion/contraction of the interfacial area on surface concentration. It is noted that there is no need for a mass balance in the bulk, because the typical surfactant loading is much higher than the CMC of the monomer. Thus, the bulk is always saturated with monomer and the effect of bulk diffusion is negligible.

First, the case of weak alveolar oscillations – corresponding to shallow breathing manoeuvres – is considered. In this case, the surface concentration never approaches Γ_{max}, so $\Gamma_m \equiv \Gamma$. Thus, a single conservation equation is required, which – when simplified by a lubrication approximation – leads to the following result (Kang *et al.* 2018; Bouchoris & Bontozoglou 2022):

$$\begin{aligned} &\frac{\partial \Gamma}{\partial t} + \frac{2\Gamma \dot{R}}{R} - \frac{1}{R^2 \sin\theta} \frac{\partial}{\partial \theta} \left(\frac{\Gamma h^2 \sin\theta}{2\mu} \frac{\partial p}{\partial \theta} - \frac{\Gamma h \sin\theta}{\mu} \frac{\partial \sigma}{\partial \theta} \right) \\ &\qquad - \frac{\mathcal{D}_s}{R^2 \sin\theta} \frac{\partial}{\partial \theta} \left(\sin\theta \frac{\partial \Gamma}{\partial \theta} \right) = j_b. \end{aligned} \tag{2.13}$$

Here, $\mathcal{D}_s$ is the surface diffusivity of surfactant and the terms in the two parentheses represent, respectively, the contributions of convection and surface diffusion. Eqaution (2.13) may take the following condensed form:

$$\frac{\partial}{\partial t} \left(2\pi R^2 \sin\theta\, \Gamma \right) + \frac{\partial Q_\Gamma}{\partial \theta} = 2\pi R^2 \sin\theta\, j_b, \tag{2.14}$$

https://doi.org/10.1017/jfm.2025.10798 Published online by Cambridge University Press

where $Q_\Gamma(\theta, t)$ is the interfacial flow rate of surfactant along the entire $\phi-$circumference

$$Q_\Gamma(\theta, t) = 2\pi R \ \sin\theta \left(u_s \Gamma - \frac{\mathcal{D}_s}{R} \frac{\partial \Gamma}{\partial \theta} \right), \tag{2.15}$$

and u_s is the interfacial water velocity

$$u_s \equiv u_\theta(R-h, \theta, t) = -\frac{1}{2\mu} \frac{\partial p}{\partial \theta} \frac{h^2}{R} + \frac{1}{\mu} \frac{\partial \sigma}{\partial \theta} \frac{h}{R}. \tag{2.16}$$

In order to describe deep-breathing manoeuvres, i.e. alveolar oscillations that include monolayer collapse and replenishment, the following modifications are necessary. As noted previously, $\sigma = \sigma(\Gamma_m)$ and $E = E(\Gamma_m)$, i.e. capillary and Marangoni forcing are both driven by the monolayer concentration and not the total surface value, Γ. Thus, convective and diffusive fluxes have as a driving force the monolayer concentration Γ_m. However, the reservoir extensions are attached to the monolayer (Parra & Perez-Gil 2015), and consequently are transported with it. Thus, for each mol of monolayer surfactant transported by convection or diffusion Γ_r/Γ_m also follow, or equivalently a total of $(\Gamma_r + \Gamma_m)/\Gamma_m = \Gamma/\Gamma_m$ is transported. As a result, the interfacial flow rate, Q_Γ, now becomes

$$\begin{aligned} Q_\Gamma(\theta, t) &= 2\pi R \ \sin\theta \left[u_s(\Gamma_m) \, \Gamma_m - \frac{\mathcal{D}_s}{R} \frac{\partial \Gamma_m}{\partial \theta} \right] \left(\frac{\Gamma}{\Gamma_m} \right) \\ &= 2\pi R \ \sin\theta \left[u_s(\Gamma_m) \, \Gamma - \frac{\mathcal{D}_s}{R} \frac{\partial \Gamma_m}{\partial \theta} \left(\frac{\Gamma}{\Gamma_m} \right) \right]. \end{aligned} \tag{2.17}$$

Implementation of the above modifications leads to the following conservation equation for the total surface concentration of surfactant:

$$\frac{\partial \Gamma}{\partial t} + \frac{2\Gamma \dot{R}}{R} - \frac{1}{R \sin\theta} \frac{\partial}{\partial \theta} \left[\sin\theta \, u_s(\Gamma_m) \, \Gamma - \sin\theta \, \frac{\mathcal{D}_s}{R} \frac{\partial \Gamma_m}{\partial \theta} \left(\frac{\Gamma}{\Gamma_m} \right) \right] = j_b, \tag{2.18}$$

with the exchange rate with the bulk given by (2.11). It is noted that the internal exchange rate j_r, given by (2.12), results only in a redistribution of surfactant between the monolayer and the reservoir, and therefore does not enter the conservation equation for the total surface concentration. However, it is critical for the correct modelling of the evolution of the monolayer concentration, Γ_m, which is described by the following expression:

$$\frac{\partial \Gamma_m}{\partial t} + \frac{2\Gamma_m \dot{R}}{R} - \frac{1}{R \sin\theta} \frac{\partial}{\partial \theta} \left[\sin\theta \, u_s(\Gamma_m) \, \Gamma_m - \sin\theta \, \frac{\mathcal{D}_s}{R} \frac{\partial \Gamma_m}{\partial \theta} \right] = j_b + j_r. \tag{2.19}$$

2.5. *Initial and boundary conditions*

The evolution of liquid film thickness and surfactant surface concentration as described by (2.1), (2.18) and (2.19) – or (2.1) and (2.13) for the simpler case of weakly nonlinear oscillations – is supplemented by appropriate initial and boundary conditions. A convenient starting point for all the computations to be presented next is the equilibrium structure of a motionless alveolus. At equilibrium, both the interface surfactant concentration and the capillary pressure are uniform in θ, and the interface attains a spherical shape with surface tension $\sigma_{eq} = \sigma_{eq}(\Gamma_{eq})$. Then, (2.1) has a trivial solution for the liquid film thickness, $H(\theta)$, which is a linear function of $\cos\theta$ determined by two parameters, the mean thickness, $\bar{H}$, and the thickness over the rim, $H(\theta_0) \equiv H_0$ (Bouchoris & Bontozoglou 2022). The computations with this initial condition indicate that in most cases a single oscillation cycle is sufficient to reach the periodic solution.

https://doi.org/10.1017/jfm.2025.10798 Published online by Cambridge University Press

The existence of a continuous, and rather thick, liquid layer over the sharp rim ($H_0 = 0.14\ \mu$m as estimated from the data of Bastacky *et al.* (1995)) is attributed to the existence of repulsive disjoining pressure forces (Starov & Ivanov 2004), which develop between the interface, the epithelium and surfactant aggregates squeezed in between. This picture is further supported by recent measurements (Xu *et al.* 2020) that estimate the combined aggregate and monolayer thickness to be of the order of 120−150 nm, i.e. in quantitative agreement with the data of Bastacky *et al.* (1995). Apart from determining H_0, the disjoining pressure has no role in the dynamics, because its characteristic time scale is very large, even compared with the breathing frequency (Oron, Davis & Bankoff 1997; Zelig & Haber 2002). The non-zero value of film thickness over the rim was shown by Bouchoris & Bontozoglou (2022) to play a key role in the development of tangential motion during the oscillation cycle.

Boundary conditions are applied at the apex, $\theta = \pi/2$, and along the rim of the alveolus at $\theta = \theta_0$. Symmetry is assumed at the alveolar apex, and thus

$$\frac{\partial h}{\partial \theta} = \frac{\partial \Gamma}{\partial \theta} = \frac{\partial \Gamma_m}{\partial \theta} = 0 \quad \text{at} \quad \theta = \pi/2. \tag{2.20}$$

It has been argued (Bouchoris & Bontozoglou 2022) that the boundary conditions along the rim are critical for correct modelling of the dynamics, as they dictate the gradients with the interior that drive the flow and transport phenomena. In the present investigation, the boundary conditions proposed by Bouchoris & Bontozoglou (2022) are used, which amount to simple mass balances that equate water and surfactant accumulation over the rim to the respective fluxes from the interior at θ_0.

In terms of the volumetric flow rate of water around the circumference of the rim, $Q(\theta_0, t)$, the mass balance of water takes the form

$$-2\,Q(\theta_0, t) = \frac{d}{\mathrm{d}t}\left[2\pi R \sin\theta_0 \left(\pi \frac{(r_0 + h_0)^2}{2} - \pi \frac{r_0^2}{2}\right)\right]. \tag{2.21}$$

Similar mass balances for the total and monolayer surfactant, taking into account convection and diffusion at the interface and exchange with the bulk and the reservoir, lead to the following expressions:

$$-2Q_\Gamma(\theta_0, t) + 2\pi R \sin\theta_0\ \pi(r_0 + h_0)\, j_b|_{\theta_0} = \frac{d}{\mathrm{d}t}\big[2\pi R \sin\theta_0\, \pi\ (r_0 + h_0)\ \Gamma_0\big], \tag{2.22}$$

$$-2Q_{\Gamma m}(\theta_0, t) + 2\pi R \sin\theta_0\ \pi(r_0 + h_0)(j_b + j_r)|_{\theta_0} = \frac{d}{\mathrm{d}t}\big[2\pi R \sin\theta_0\, \pi\ (r_0 + h_0)\ \Gamma_{m0}\big]. \tag{2.23}$$

The multiplier two in. (2.21), (2.22) and (2.23) accounts for flux coming to the rim from both sides of the mid-alveolar wall and is appropriate for alveoli in close packing (type A alveoli), as they occur in the lowest respiratory bronchioles. The minus sign indicates flow in the negative θ-direction, i.e. towards the rim.

The application of mass balances only – and not flow equations – over the rim is based on the assumption that the rim dynamics does not influence the problem, or, in other words, that it is totally enslaved to the dynamics of the alveolus. This assumption has been justified by an order-of-magnitude analysis, which revealed that Marangoni forcing is much faster than capillary drainage (Bouchoris & Bontozoglou 2022). Thus, the flow induced inside the alveolus by Marangoni stresses dominates the system dynamics.

https://doi.org/10.1017/jfm.2025.10798 Published online by Cambridge University Press

3. Scaling and numerical solution

3.1. *The final equations in dimensionless form*

The characteristic scales used to non-dimensionalise the problem variables are taken from the equilibrium conditions. Thus, we consider a motionless alveolar cap of radius $\bar{R}$, coated by a liquid film whose mean thickness is $\bar{H}$. With these choices, the lubrication parameter is formally defined as

$$\epsilon = \frac{\bar{H}}{\bar{R}}. \tag{3.1}$$

The liquid is loaded by surfactant aggregates and equilibrates with an adsorbed monolayer of surface concentration Γ_{eq}, which results in surface tension σ_{eq} and surface elasticity $E_{eq} = -\Gamma_{eq}\ (\mathrm{d}\sigma/\mathrm{d}\Gamma)|_{\Gamma=\Gamma_{eq}}$. Finally, the characteristic time is the breathing period, T.

With the above scales, the following dimensionless variables are defined: $h^* = h/\bar{H}$, $H^* = H/\bar{H}$, $R^* = R/\bar{R}$, $r_0^* = r_0/\bar{R}$, $t^* = t/T$, $\Gamma^* = \Gamma/\Gamma_{eq}$, $\sigma^* = \sigma/\sigma_{eq}$, $E^* = E/E_{eq}$, $p^* = p\,\bar{R}^2/(\sigma_{eq}\bar{H})$, $j_b^* = j_b T/\Gamma_{eq}$ and $j_r^* = j_r T/\Gamma_{eq}$. The governing evolution equations are transformed as follows in terms of the dimensionless variables:

$$\frac{\partial h^*}{\partial t^*} + \frac{2h^*\dot{R}^*}{R^*} + \frac{1}{R^{*2}\sin\theta}\frac{\partial Q^*}{\partial \theta} = 0, \tag{3.2}$$

$$\frac{\partial \Gamma^*}{\partial t^*} + \frac{2\Gamma^*\dot{R}^*}{R^*} + \frac{1}{R^{*2}\sin\theta}\frac{\partial Q_\Gamma^*}{\partial \theta} - j_b^* = 0, \tag{3.3}$$

and

$$\frac{\partial \Gamma_m^*}{\partial t^*} + \frac{2\Gamma_m^*\dot{R}^*}{R^*} + \frac{1}{R^{*2}\sin\theta}\frac{\partial Q_{\Gamma m}^*}{\partial \theta} - (j_b^* + j_r^*) = 0. \tag{3.4}$$

Terms Q^*, Q_Γ^*, $Q_{\Gamma m}^*$ are respectively the dimensionless volumetric flow rates of water, and total and monolayer surfactant, the former scaled by $\bar{Q} = 2\pi\bar{R}^2\bar{H}/T$ and the two latter by $\bar{Q}_{\Gamma,eq} = 2\pi\bar{R}^2\Gamma_{eq}/T$.

Three trivial algebraic manipulations are undertaken in order to derive the final evolution equations from ((3.2)–(3.4)). First, the independent spatial variable θ is replaced by $x = -\cos\theta$. Second, the fluxes of water and surfactant are expanded according to the expressions in (2.1), (2.15) and (2.17), using also (2.2) and (2.16) for the pressure and the surface velocity. Third, to avoid symbol overload, the dimensionless variables are written from now on without the asterisk, e.g. h signifies h^*, Γ signifies Γ^*, R signifies R^* etc. There should be no confusion with this last change, since only dimensionless variables appear in the rest of the paper.

Thus, the final evolution equations are

$$\frac{\partial h}{\partial t} + \frac{2h\dot{R}}{R} + \frac{1}{R^2}\frac{\partial Q}{\partial x} = 0, \tag{3.5}$$

$$\frac{\partial \Gamma}{\partial t} + \frac{2\Gamma\dot{R}}{R} + \frac{1}{R^2}\frac{\partial Q_\Gamma}{\partial x} - j_b = 0, \tag{3.6}$$

and

$$\frac{\partial \Gamma_m}{\partial t} + \frac{2\Gamma_m\dot{R}}{R} + \frac{1}{R^2}\frac{\partial Q_{\Gamma m}}{\partial x} - (j_b + j_r) = 0, \tag{3.7}$$

https://doi.org/10.1017/jfm.2025.10798 Published online by Cambridge University Press

which are solved for initial conditions

$$h(x,0)=H(x),\qquad \Gamma(x,0)=\Gamma_m(x,0)=1, \tag{3.8}$$

and subject to the following boundary conditions at $x_0=-\cos\theta_0$, with subscript 0 signifying value at the rim:

$$-2\,Q(x_0,t)=\sqrt{1-x_0^2}\,\pi R\left[(r_0+\epsilon h_0)\,\frac{\mathrm{d}h_0}{\mathrm{d}t}+h_0\left(r_0+\epsilon\frac{h_0}{2}\right)\frac{\dot R}{R}\right], \tag{3.9}$$

$$-2\,Q_\Gamma(x_0,t)=\sqrt{1-x_0^2}\,\pi R\left[(r_0+\epsilon h_0)\left(\frac{\mathrm{d}\Gamma_0}{\mathrm{d}t}-j_{b0}\right)+\epsilon\Gamma_0\frac{\mathrm{d}h_0}{\mathrm{d}t}+\Gamma_0(r_0+\epsilon h_0)\frac{\dot R}{R}\right], \tag{3.10}$$

$$-2\,Q_{\Gamma m}(x_0,t)=\sqrt{1-x_0^2}\,\pi R\left[(r_0+\epsilon h_0)\left(\frac{\mathrm{d}\Gamma_{m0}}{\mathrm{d}t}-j_{b0}-j_{r0}\right)+\epsilon\Gamma_{m0}\frac{\mathrm{d}h_0}{\mathrm{d}t}+\Gamma_{m0}(r_0+\epsilon h_0)\frac{\dot R}{R}\right]. \tag{3.11}$$

The symmetry boundary conditions at $\theta=\pi$ are now trivially satisfied, provided the derivatives $\partial h/\partial x,\ \partial\Gamma/\partial x,\ \partial\Gamma_m/\partial x$ are finite at $x=1$.

The fluxes that appear in ((3.5)–(3.7)) are given in expanded form by the following expressions:

$$Q=\epsilon^3\frac{Ca^{-1}}{3R^4}\sigma(\Gamma_m)h^3\left(1-x^2\right)\frac{\partial}{\partial x}(2h+g)-\epsilon\frac{Ma}{2R^2}h^2\left(1-x^2\right)\frac{E(\Gamma_m)}{\Gamma_m}\frac{\partial\Gamma_m}{\partial x}, \tag{3.12}$$

$$\begin{aligned}Q_\Gamma=&\epsilon^3\frac{Ca^{-1}}{2R^4}\Gamma\sigma(\Gamma_m)h^2\left(1-x^2\right)\frac{\partial}{\partial x}(2h+g)-\epsilon\frac{Ma}{R^2}\Gamma h\left(1-x^2\right)\frac{E(\Gamma_m)}{\Gamma_m}\frac{\partial\Gamma_m}{\partial x}\\&-\frac{Pe_s^{-1}}{R^2}\left(1-x^2\right)\frac{\partial\Gamma_m}{\partial x}\left(\frac{\Gamma}{\Gamma_m}\right),\end{aligned} \tag{3.13}$$

$$\begin{aligned}Q_{\Gamma m}=&\epsilon^3\frac{Ca^{-1}}{2R^4}\Gamma_m\,\sigma(\Gamma_m)h^2\left(1-x^2\right)\frac{\partial}{\partial x}(2h+g)\\&-\epsilon\frac{Ma}{R^2}\Gamma_m\,h\left(1-x^2\right)\frac{E(\Gamma_m)}{\Gamma_m}\frac{\partial\Gamma_m}{\partial x}-\frac{Pe_s^{-1}}{R^2}\left(1-x^2\right)\frac{\partial\Gamma_m}{\partial x},\end{aligned} \tag{3.14}$$

$$j_b=St_b\left[(\Gamma_{m,\infty}-\Gamma_m)-\frac{\Gamma_m}{KC_{10}}\right], \tag{3.15}$$

$$j_r=St_r(\Gamma_{m,\infty}-\Gamma_m)(\Gamma-\Gamma_m)-St_{rc}\frac{1}{(\Gamma_{max}-\Gamma_m)^2}, \tag{3.16}$$

where, as a reminder, the properties σ and E in (3.12)–(3.14) are written with the dependence on monolayer concentration made explicit. It is noted that the function $g(x,t)$, which appears in these expansions, is a substitution for the expression

$$g(x,t)=\frac{\partial}{\partial x}\left(\left(1-x^2\right)\frac{\partial h}{\partial x}\right). \tag{3.17}$$

This substitution is necessary for the finite-element solution of the problem, as the introduction of the new unknown function $g(x,t)$ eliminates the higher than second-order derivatives in h. Finally, the dimensionless numbers that appear in (3.12)–(3.16)

https://doi.org/10.1017/jfm.2025.10798 Published online by Cambridge University Press

are defined as follows:

$$Ca^{-1} = \frac{\sigma_{eq}}{\mu(\bar{R}/T)}, \quad Ma = \frac{E_{eq}}{\mu(\bar{R}/T)}, \quad Pe_s^{-1} = \frac{\mathcal{D}_s T}{\bar{R}^2},$$
$$St_b = \frac{T}{1/(k_{ads} C_{10})}, \quad St_r = \frac{T}{1/(k_r \Gamma_{eq})}, \quad St_{rc} = \frac{T}{\Gamma_{eq}^3/k_{rc}}, \tag{3.18}$$

and may be viewed as ratios of the breathing period to the characteristic times of capillary, Marangoni, diffusion, adsorption and replenishment phenomena.

3.2. *Numerical solution*

The evolution equations ((3.5)–(3.7)) are discretised in space with a Galerkin finite-element method. The nodes of the independent spatial variable $x \in [x_0, 1]$ are clustered close to x_0, where the solution changes faster. Within each element, the primary unknowns, h, g, Γ, Γ_m, are expanded by quadratic Lagrangian basis functions, ϕ_i, and the evolution equations are weighted integrally with the same basis functions. The final weak forms are as follows, after applying integration by parts to reduce the order of differentiation:

$$\int_{x_0}^{1} \frac{\partial h}{\partial t}\phi_i \,\mathrm{d}x + \int_{x_0}^{1} \frac{2h\dot{R}}{R}\phi_i \,\mathrm{d}x + \frac{1}{R^2}\left[Q\phi_i\right]_{x_0}^{1} - \frac{1}{R^2}\int_{x_0}^{1} Q\frac{d\phi_i}{\mathrm{d}x}\,\mathrm{d}x = 0, \tag{3.19}$$

$$\int_{x_0}^{1} g\,\phi_i \,\mathrm{d}x - \left[\left(1-x^2\right)\frac{\partial h}{\partial x}\phi_i\right]_{x_0}^{1} + \int_{x_0}^{1}\left(1-x^2\right)\frac{\partial h}{\partial x}\frac{d\phi_i}{\mathrm{d}x}\,\mathrm{d}x = 0, \tag{3.20}$$

$$\int_{x_0}^{1} \frac{\partial \Gamma}{\partial t}\phi_i \,\mathrm{d}x + \int_{x_0}^{1} \frac{2\Gamma\dot{R}}{R}\phi_i \,\mathrm{d}x + \frac{1}{R^2}\left[Q_\Gamma\phi_i\right]_{x_0}^{1} - \frac{1}{R^2}\int_{x_0}^{1} Q_\Gamma\frac{d\phi_i}{\mathrm{d}x}\,\mathrm{d}x - \int_{x_0}^{1} j_b\phi_i \,\mathrm{d}x = 0, \tag{3.21}$$

and

$$\int_{x_0}^{1} \frac{\partial \Gamma_m}{\partial t}\phi_i \,\mathrm{d}x + \int_{x_0}^{1} \frac{2\Gamma_m\dot{R}}{R}\phi_i \,\mathrm{d}x + \frac{1}{R^2}\left[Q_{\Gamma m}\phi_i\right]_{x_0}^{1} - \frac{1}{R^2}\int_{x_0}^{1} Q_{\Gamma m}\frac{d\phi_i}{\mathrm{d}x}\,\mathrm{d}x - \int_{x_0}^{1}(j_b + j_r)\phi_i \,\mathrm{d}x = 0. \tag{3.22}$$

The fluxes in the integrated terms in (3.19)–(3.22) are by symmetry equal to zero at $x = 1$, and are evaluated at $x = x_0$ from the boundary conditions, (3.9)–(3.11). Time derivatives are treated with an implicit Euler scheme and the spatial integrals are evaluated by three-point Gaussian quadrature. Finally, the resulting system of nonlinear algebraic equations is solved with a Newton–Raphson iterative scheme.

4. Results

The results presented in the rest of the paper are computed using the following parameter values. The equilibrium alveolar radius and the septum thickness at the rim are $\bar{R} = 100\,\mu\mathrm{m}$ and $2r_0 = 4\,\mu\mathrm{m}$, respectively (Ochs *et al.* 2004). Alveolar oscillations are purely sinusoidal, characterised by the dimensionless amplitude, a, i.e. in dimensionless terms

$$R(t) = 1 + a\sin(2\pi t)\,. \tag{4.1}$$

https://doi.org/10.1017/jfm.2025.10798 Published online by Cambridge University Press

The liquid layer has the density and viscosity of pure water at the physiological temperature of 37 °C. At equilibrium, its mean thickness is $\bar{H} = 0.3\ \mu\text{m}$ and its thickness over the rim is $H_0 = 0.14\ \mu\text{m}$ (Bastacky *et al.* 1995; Xu *et al.* 2020). The equilibrium surface tension is taken as $\sigma_{eq} = 0.023\ \text{N m}^{-1}$, the molar surface area at zero surface pressure $\Omega_0 = 3.0 \times 10^5\ \text{m}^2\ \text{mol}^{-1}$ and the intrinsic compressibility $\alpha = 0.0052\ \text{m mN}^{-1}$ (Wüstneck *et al.* 2005; Zuo *et al.* 2016). Surfactant exchange between the monolayer and the bulk is quantified by the adsorption parameter $k_{ads}C_{10}$. Its value is zero for the case of an insoluble surfactant and takes typical values in the range $k_{ads}C_{10} = 10{-}40\ \text{s}^{-1}$ for soluble surfactants (Zuo *et al.* 2005; Saad *et al.* 2010; Bouchoris & Bontozoglou 2021). The rate of monolayer replenishment from the reservoir during alveolar expansion is taken as $k_r = 150\ \text{m}^2\ \text{mol}^{-1}\ \text{s}^{-1}$. The values of σ_{eq}, $k_{ads}C_{10}$, α and k_r are derived from best fit with available experimental data, as described in Appendix A. The parameter k_{rc} that quantifies how abruptly the monolayer concentration arrests at the value Γ_{max} during monolayer collapse is set to $k_{rc} = 10^{-5}\ \text{mol}^3\ \text{m}^{-6}\ \text{s}^{-1}$.

It is noted that there is a high degree of confidence in the accuracy of the selected parameter values, for two reasons. First, each parameter affects the data (the surface tension–surface area loop) in a different way. For example σ_{eq} moves the entire loop up or down, $k_{ads}C_{10}$ varies the width of the loop, α modifies the slope of the compression leg and k_r restricts the upper limit of the loop. Thus, there is a single combination of best-fit parameter values. Second, the values selected 'blindly' by the above procedure are in very satisfactory agreement with the literature. For example, all measured data of equilibrium surface tension are in the range $\sigma_{eq} = 22{-}25\ \text{mN m}^{-1}$, independent from the total surfactant concentration (Wüstneck *et al.* 2005; Parra & Perez-Gil 2015). Also, the best-fit value of the monolayer compressibility, α, is in the expected range for the tilted condensed regime and – most important – in agreement with the compressibility of a pure DPPC monolayer (Schürch *et al.* 1998; Possmayer *et al.* 2001; Zhang *et al.* 2011).

4.1. *The dynamics of large-amplitude oscillations*

The onset of monolayer collapse when $\Gamma \to \Gamma_{max}$ occurs at oscillation amplitudes $a \approx 0.05{-}0.08$, with the exact value depending on the minimum surface tension achievable by compression, $\sigma_{min} = \sigma(\Gamma_{max})$, and on the surfactant solubility. The value of minimum surface tension used throughout the paper is $\sigma_{min} = 0.005\ \text{N m}^{-1}$ and the dynamics of the system is first examined for an insoluble surfactant.

An overview of the behaviour of the alveolus is provided by figure 3, which shows the temporal variation of Γ and Γ_m for two oscillation cycles starting from rest at equilibrium. It is confirmed that the variation of surface surfactant concentration is mainly driven by the change in the alveolar surface area and thus is 180° out of phase with the oscillation amplitude. The spatial variation of Γ and Γ_m (the latter responsible for the generation of Marangoni stresses) is too small to be visually distinguished in such a plot, so the depicted behaviour is valid for all points along the alveolar interface.

Figure 3(*a*) refers to oscillations with an amplitude ($a = 0.05$) which is too small to cause monolayer collapse. Thus, the curves for Γ and Γ_m are superimposed. The situation is different in figure 3(*b*), where the oscillation amplitude is $a = 0.15$. During compression, the total surface concentration increases continuously while the monolayer concentration is saturated at $\Gamma_m = 1.1465$, i.e. $\approx 15\,\%$ higher than the equilibrium value. During re-expansion, the monolayer is enriched by transport from the reservoir, which is eventually consumed leaving once again a pure monolayer ($\Gamma = \Gamma_m$).

For small-amplitude oscillations, Bouchoris & Bontozoglou (2022) developed expansions up to second order in the amplitude of the following general form for variables

https://doi.org/10.1017/jfm.2025.10798 Published online by Cambridge University Press

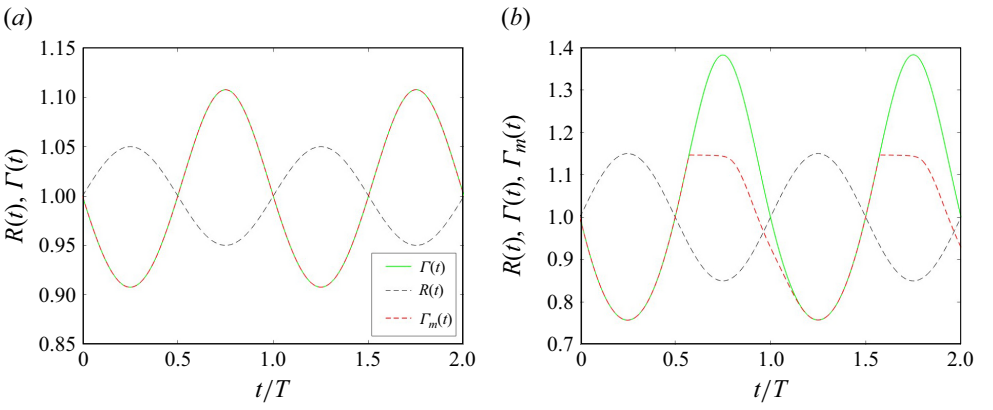


Figure 3. The temporal variation of alveolar radius $R(t)$ (black dashed line), monolayer concentration Γ_m (red dashed line) and total surface concentration Γ (green solid line) for oscillations with amplitude (*a*) $a = 0.05$ and (*b*) $a = 0.15$.

of interest such as surface deformation, $h(x, t)$, surface velocity, $u_s(x, t)$, volumetric flow rate, $Q(x, t)$ and wall shear stress, $\tau_w(x, t)$:

$$\Phi(x, t) = a\,\mathrm{Re}\big[\Phi_1(x)\, e^{i2\pi t}\big] + a^2\Big(\mathrm{Re}\big[\Phi_2(x)\, e^{i4\pi t}\big] + \Phi_{2s}(x)\Big). \tag{4.2}$$

The analytic expressions for the amplitudes in terms of the system parameters are contained in the original publication. Given that the linear/weakly nonlinear solution is relatively simple, and that it has already been used to provide predictions beyond its formal range of validity (Livanos *et al.* 2024), it is of interest to compare it with the full numerical solution.

Numerical results for the surface velocity are computed from (2.16), for the volumetric flow rate from (2.3) and for the wall shear stress from the following expression (Bouchoris & Bontozoglou 2022):

$$\tau_w = \frac{h}{R}\frac{\partial p}{\partial \theta} - \frac{1}{R}\frac{\partial \sigma}{\partial \theta}. \tag{4.3}$$

Indicative numerical results for oscillation amplitude $a = 0.0325$ are Fourier transformed and the magnitudes of the first two harmonics are compared with the weakly nonlinear predictions in figure 4(*a*,*b*). It is observed that numerics and asymptotics are in close agreement. The gross characteristics of $h(x, t)$, $u_s(x, t)$, $Q(x, t)$ and $\tau_w(x, t)$ as the oscillation amplitude increases, and the extent to which they may be roughly estimated from the linear prediction, are examined in more detail in Appendix B.

A key characteristic of the dynamics of the present problem – already discussed in the linear limit by Bouchoris & Bontozoglou (2022) – is the contrast between the dominance of Marangoni stresses along the interface and the significant role of capillary and viscous stresses in the interior of the film. Thus, although $Ma >> Ca^{-1}$, all contributions must be retained for correct prediction of the flow.

The dominance of Marangoni over capillary stresses on the interface results in the instantaneous establishment of an inverse Marangoni flow (Manikantan & Squires 2020) that negates the effect of variations in interfacial curvature. This behaviour is witnessed by the spatial distribution of the monolayer concentration of surfactant, which is depicted in figure 5(*a*,*b*). In order to include results for a number of representative time instants, we actually plot the difference $(\Gamma_m(x, t) - \Gamma_m(1, t))$, normalised with the oscillation amplitude a, so that all the curves coincide at the apex. The oscillatory shape of these

https://doi.org/10.1017/jfm.2025.10798 Published online by Cambridge University Press

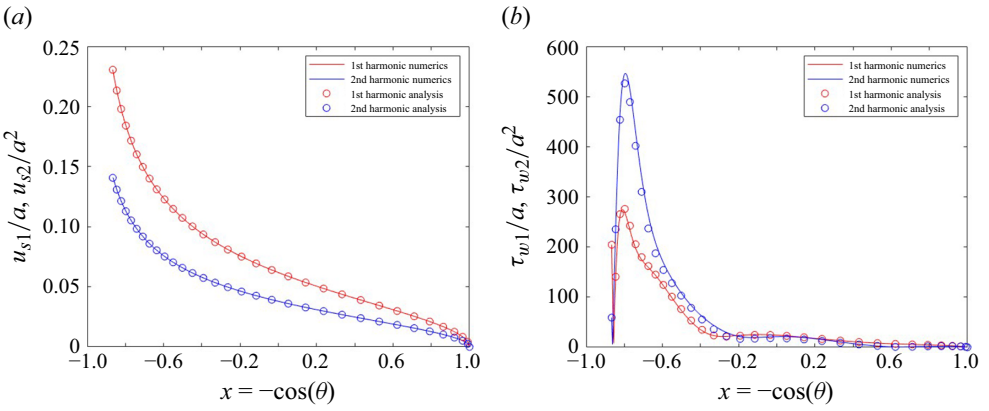


Figure 4. The first and second harmonics of the numerical solution (continuous lines) compared with the weakly nonlinear predictions (open circles).

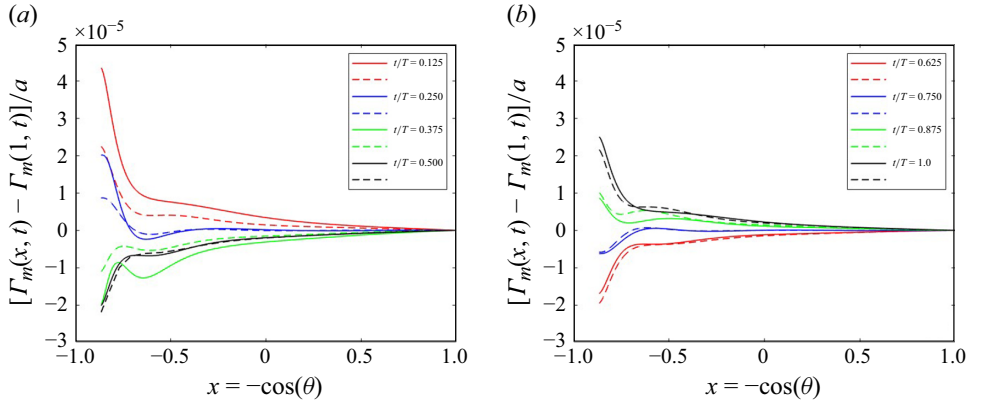


Figure 5. The term $[\Gamma_m(x,t) - \Gamma_m(1,t)]/a$ for time instants $t/T = 0.125$ (red), 0.25 (blue), 0.375 (green) and 0.50 (black) in panel (a) and $t/T = 0.625$ (red), 0.75 (blue), 0.875 (green) and 1.0 (black) in panel (b). The alveolar oscillations have amplitude $a = 0.05$ (dashed lines) and 0.20 (continuous lines).

curves occurs in response to variations of interfacial curvature, and is contrasted with the monotonic change of $u_s(x,t)$ with x in figure 4(a).

The results in figure 5 are qualitatively similar for the relatively small oscillation amplitude $a = 0.05$ (dashed lines) and for $a = 0.20$ (continuous lines), despite the extensive monolayer collapse during compression that occurs in the second case. The behaviour indicates that the limitation imposed on Γ_m due to the collapse does not obstruct the spatial variations that give rise to Marangoni stresses. This happens because the necessary gradients are very small and the modelling of collapse by (2.12) allows for them to develop. Restriction of the spatial gradients of Γ_m and of the ensuing Marangoni stresses occurs only for extremely small values of the parameter k_{rc}, which determines the stiffness of the monolayer. This behaviour is depicted in figure 6, which shows the temporal maxima of the surface velocity, u_s, along the liquid film for different values of k_{rc}. It is observed that the Marangoni-induced surface flow is significantly affected only below $k_{rc} = 10^{-6}$. The results presented in the rest of the paper are computed using $k_{rc} = 10^{-5}$ and the role of k_{rc} is not further investigated, given the apparent lack of measured data.

https://doi.org/10.1017/jfm.2025.10798 Published online by Cambridge University Press

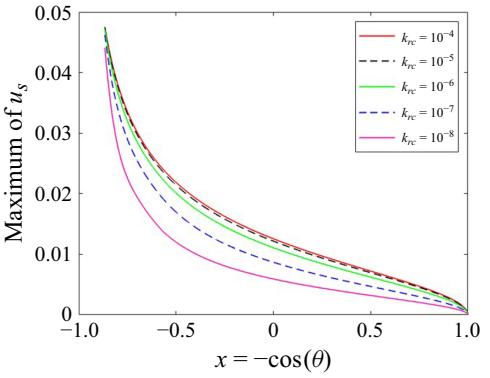


Figure 6. The maxima of surface velocity for oscillations with amplitude $a = 0.20$ and monolayer stiffness parameter $k_{rc} = 10^{-4}$, 10^{-5}, 10^{-6}, 10^{-7} and 10^{-8} (red, black dashed, green, blue dashed and purple lines, respectively).

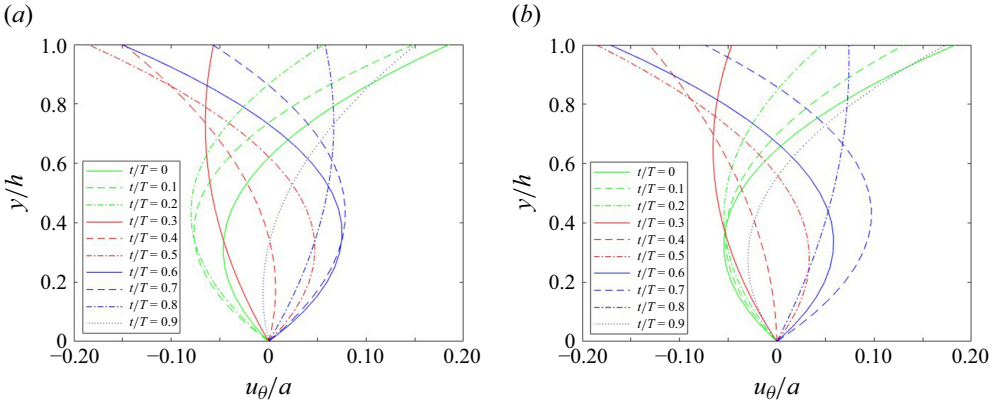


Figure 7. The profile of tangential velocity, u_θ, normalised with the oscillation amplitude a, inside the liquid layer, plotted for different time instants during a breathing cycle: (*a*) $a = 0.01$ and (*b*) $a = 0.20$.

Although the main flow variables appear to scale roughly with the oscillation amplitude, there are important modifications with increasing nonlinearity and in particular with the onset of monolayer collapse. A first impression is provided by considering the tangential velocity field inside the liquid layer. Figure 7(*a*,*b*) shows (u_θ/a) for equidistant time instants during a breathing cycle for $a = 0.01$ and $a = 0.20$, respectively. The similarity of figure 7(*a*) to an inverted Stokes layer is evident, with the main difference being that the motion is now triggered not by tangential oscillation of the wall but by the effect of Marangoni stresses. Another important difference is that momentum transfer from the surface towards the wall is affected not only by viscosity but also by capillary pressure, induced on the free surface by local variation of curvature.

Recalling that Marangoni stresses are triggered by the periodic variation of the monolayer concentration inside the alveolus, the symmetric shape of figure 7(*a*) is explained by the fact that, in the linear limit, the variation in wall surface area is proportional to the oscillation amplitude. Thus, the change in surface tension is symmetric during expansion and contraction of the alveolus. However, this symmetry breaks with increasing oscillation amplitude as $O(a^2)$ effects come into play. Then, the decrease in surface area during contraction is less than the increase during expansion, and capillary

https://doi.org/10.1017/jfm.2025.10798 Published online by Cambridge University Press

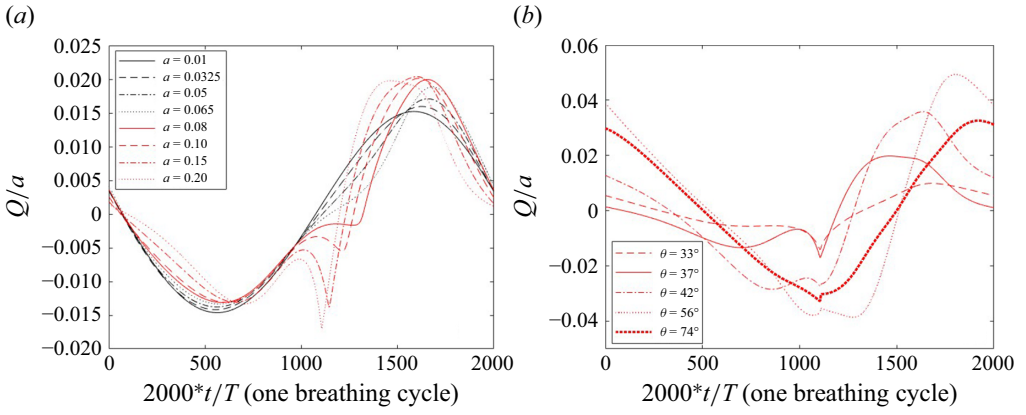


Figure 8. (*a*) The temporal variation of volumetric flow rate at $\theta \approx 37°$ during one breathing cycle for $k_{ads}C_{10} = 0\,s^{-1}$. Black lines are for $a = 0.01$ (continuous), 0.0325 (dashed), 0.05 (dash-dotted) and 0.065 (dotted). Red lines are for $a = 0.08$ (continuous), 0.10 (dashed), 0.15 (dash-dotted) and 0.20 (dotted). (*b*) The temporal variation of volumetric flow rate for $a = 0.20$ at locations $\theta \approx 33°$ (dashed), 37° (continuous), 42° (dash-dotted), 56° (dotted) and 74° (thick dots).

pressure introduces asymmetry. The effect intensifies much more with the onset of monolayer collapse, because then the surface tension, instead of varying in response to the change in surface area, remains constant at $\sigma_{min} = \sigma(\Gamma_{max})$. The asymmetric variation of the velocity profile for $a = 0.20$ is depicted in figure 7(*b*).

Sensitive indicators of the effects of viscosity and capillarity on the transmission of momentum through the liquid film are the volumetric flow rate, Q, and the wall shear stress, τ_w. Thus, figures 8(*a*,*b*) and 9(*a*,*b*) respectively plot data for the temporal variation of Q and τ_w, during one breathing cycle. Figures 8(*a*) (for Q) and 9(*a*) (for τ_w) refer to a single location close to the alveolar rim at $\theta \approx 37°$. Black lines correspond to amplitudes $a = 0.01-0.065$ that do not reach monolayer collapse, and red lines to amplitudes $a = 0.08-0.20$ that cause collapse. In the linear limit (continuous black lines) both variations of Q and τ_w are sinusoidal, i.e. perfectly symmetric in time. Asymmetry develops gradually with increasing amplitude in the compression part of the cycle and, with the onset of collapse, the flow rate abruptly decelerates and then for a short time changes direction. Similar abrupt change (a spike of short duration) is observed in figure 9(*a*) in the wall shear stress. The disturbances in Q and τ_w intensify with the increase in oscillation amplitude, but magnification of the data shows that there is no discontinuity in slope.

Figures 8(*b*) and 9(*b*) depict respectively the temporal variations of Q and τ_w for a number of locations $\theta \approx 33°$, 37°, 42°, 56° and 74° and show that the spikes are more intense close to the rim, but are also observed, with diminishing intensity, deeper inside the alveolus. The strong effect of nonlinearity may be appreciated by recalling that, in the linear limit, all the curves in figures 8(*b*) and 9(*b*) would be simple sinusoids of different amplitudes.

The sudden variation in wall shear stress during deep breathing, which is related to the onset of monolayer collapse and has a short time scale compared with the breathing period, appears to increase significantly the complexity in the temporal variation of shear forces on the epithelium compared with a simple sinusoid. In addition, the expected random variation in oscillation amplitude during consecutive breathing cycles will further increase the shear stress variability both in magnitude and in phase. This behaviour may have an interesting physiological effect, as discussed in the Concluding Remarks.

https://doi.org/10.1017/jfm.2025.10798 Published online by Cambridge University Press

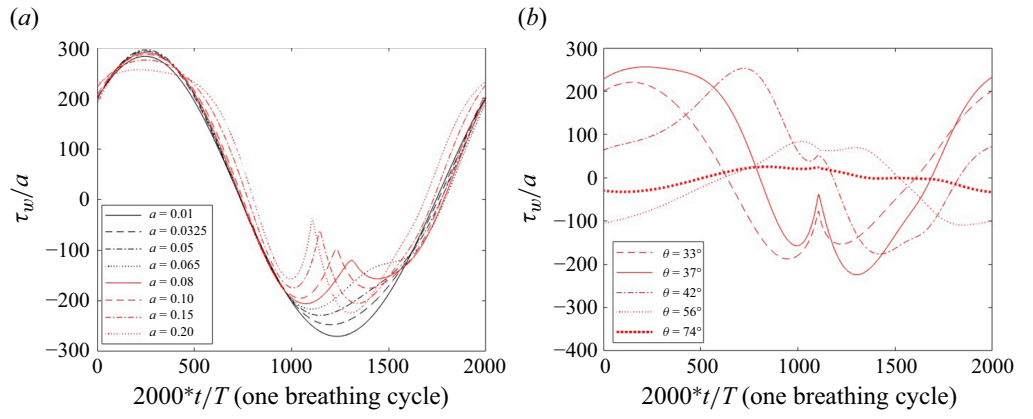


Figure 9. (*a*) The temporal variation of wall shear stress at $\theta \approx 37°$ during one breathing cycle for $k_{ads}C_{10} = 0\,\mathrm{s}^{-1}$. Black lines are for $a = 0.01$ (continuous), 0.0325 (dashed), 0.05 (dash-dotted) and 0.065 (dotted). Red lines are for $a = 0.08$ (continuous), 0.10 (dashed), 0.15 (dash-dotted) and 0.20 (dotted). (*b*) The temporal variation of wall shear stress for $a = 0.20$ at locations $\theta \approx 33°$ (dashed), 37° (continuous), 42° (dash-dotted), 56° (dotted) and 74° (thick dots).

The analysis up to this point referred to insoluble surfactant. For soluble surfactant with $k_{ads}C_{10} \sim 10{-}40\,\mathrm{s}^{-1}$, the characteristic time of exchange between the monolayer and the bulk is $t_{ads} \sim 10^{-1}{-}10^{-2}\,s$, which is much slower than the characteristic times of capillary and Marangoni flows, cf. (3.18). As a result, solubility has negligible effect at leading order and the results for the main flow parameters presented above retain the same qualitative character with relatively minor quantitative changes. Thus, they are not deemed worth reproducing. However, surfactant solubility has a significant effect on second-order phenomena to be considered next, namely the slow displacement of nanoparticles deposited on the liquid layer and the drift of surfactant through the alveolar opening.

4.2. *Alveolar clearance of insoluble particles*

Small particles contained in the inhaled air are transported distally into the lungs and many of them deposit. Clearance of insoluble particles, deposited from the trachea down to the respiratory bronchioles, occurs relatively fast (a large fraction is cleared within a few hours) through the well-studied mucociliary escalator mechanism (Smith, Eamonn & Blake 2008). Alveolar clearance is many orders of magnitude slower and its mechanism is still open to investigation. Experiments with human volunteers who inhaled $\sim$1 μm diameter fused aluminosilicate particles (Bailey *et al.* 1982, 1985) showed that the particles, which were retained after six days, cleared at a rate described by a two-component exponential function, the first component with a half-time of tens of days and the second with a half-time of hundreds of days.

Potential routes of alveolar clearance are surface transport from the alveoli to the ciliated regions of the lung and/or translocation through the epithelium and secretion by the lymphatic system (Lippmann, Yeates & Albert 1980; Oberdoerster 1988). Phagocytosis by alveolar macrophages is a major mechanism of large particle arrest, although the macrophages must also be eventually transported to ciliated regions. However, phagocytosis appears to be far less efficient for particles of nanometre size (Oberdoerster 1988; Ferin 1994). The role of surface tension, in combination with its variations induced by the breathing manoeuvres, has been hypothesised long ago as the main transport

https://doi.org/10.1017/jfm.2025.10798 Published online by Cambridge University Press

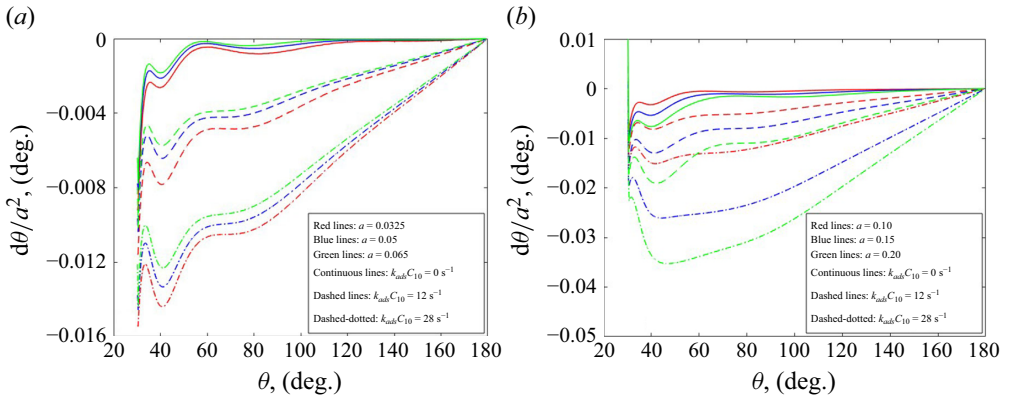


Figure 10. The displacement of a floating nanoparticle after one breathing cycle, as function of the initial deposition location, computed for surfactant solubilities $k_{ads}C_{10} = 0\ \mathrm{s}^{-1}$ (continuous lines), $k_{ads}C_{10} = 12\ \mathrm{s}^{-1}$ (dashed lines) and $k_{ads}C_{10} = 28\ \mathrm{s}^{-1}$ (dashed–dotted lines). (*a*) Small oscillation amplitudes $a = 0.0325$ (red), 0.05 (blue) and 0.065 (green). (*b*) Large oscillation amplitudes $a = 0.10$ (red), 0.15 (blue) and 0.20 (green).

mechanism (Kilburn 1968). However, this hypothesis could not be tested further because of the limited understanding of the fluid dynamics involved.

The present model provides an opportunity to investigate whether the flow inside the alveolus has a clearance effect. To this end, light, insoluble nanoparticles are assumed to stay on the surface of the liquid layer and to behave as passive tracers. Their net displacement per breathing cycle is thus computed by integrating in time the equation of motion in the lubrication limit, $u_{\theta,s}\,\mathrm{d}t = R\,d\theta$, by a fourth-order Runge–Kutta scheme. The results are expressed as displacement angle from the initial position, normalised with the square of the amplitude, and are presented in figure 10(*a*,*b*) for insoluble surfactant (continuous lines) and for surfactants with $k_{ads}C_{10} = 12\ \mathrm{s}^{-1}$ (dashed lines) and $k_{ads}C_{10} = 28\ \mathrm{s}^{-1}$ (dashed–dotted lines).

Figure 10(*a*) refers to finite but relatively small oscillation amplitudes, i.e. calm breathing. The variation with amplitude appears as an $O(a^2)$ effect, with this dependence slightly weakening with increasing a. The most interesting findings are that (i) under all conditions, particle drift is negative, i.e. all particles move toward the rim, and (ii) that increased surfactant solubility strongly intensifies the clearance rate. In general, the drift is more intense in the first 50° from the alveolar opening and maximises right on the rim. The local maximum very close to the rim, which is more pronounced at high solubilities and corresponds to a minimum in the absolute value of drift, is expected to contribute to the local accumulation of particles.

Figure 10(*b*) refers to large-amplitude oscillations, i.e. deep breathing, and the strong positive effect of surfactant solubility on clearance rate is again confirmed. However, there are two major differences from figure 10(*b*). First, there is now a positive effect of oscillation amplitude (beyond the $O(a^2)$ dependence), which intensifies with solubility. Second, with increasing oscillation amplitude the displacement at the rim decreases and in some cases (small solubility, large amplitude) becomes even positive. This means that, in those cases, particles at the rim may be temporarily obstructed by the flow from entering the alveolar ducts. However, given that particle displacements are still very small and thus clearance time scales remain of the order of many tens or hundreds of days, the high-amplitude results are not considered any further (no one can breath deeply all day long and for many days).

https://doi.org/10.1017/jfm.2025.10798 Published online by Cambridge University Press

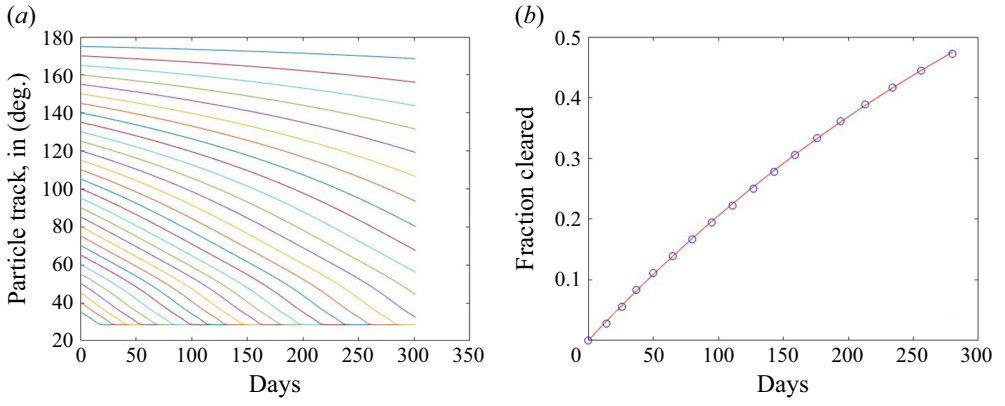


Figure 11. (*a*) The trajectory with time of particles initially equi-distributed inside the alveolus, for surfactant solubility $k_{ads}C_{10} = 28\,\mathrm{s}^{-1}$ and oscillation amplitude $a = 0.0325$. (*b*) The fraction of particles that have reached the rim versus time (blue circles) and an exponential fit with half-life 301 days (red line).

The information contained in figure 10(*a*) may be utilised directly to compute the locations of passive tracers after a large number of breathing cycles. Figure 11(*a*) shows the drift of particles, initially equi-distributed azimuthally, during the passage of 300 days, when $k_{ads}C_{10} = 28$ and $a = 0.0325$ ($\pm 10\,\%$ variation of acinar volume from the rest value). The fraction of particles that have reached the rim (considered cleared from the alveolus) is plotted in figure 11(*b*) versus time (circles) and is shown to obey an exponential variation (red line) with half-life $\tau_{1/2} = 301$ days. This value appears very small when compared with the time scale of 1–2 days for clearance of the conducting airways (nasal passages and tracheobronchial tree). However, it is in quantitative agreement with the results of *in vivo* experiments with insoluble particles by Bailey *et al.*, which gave alveolar clearance half-times of 320 (Bailey, Frances & James 1982) and 350 days (Bailey, Fry & James 1985).

A second exponential decay with much shorter half-time ($\tau_{1/2} \sim 10^1$) is expected to occur if, on top of the uniform distribution, there is an additional amount of particles deposited close to the alveolar entrance. Indeed, there is experimental evidence for such behaviour (Zeltner *et al.* 1991), which was also mechanistically interpreted as a result of interaction of the ductal airflow with recirculating flow inside the alveolus (Henry & Tsuda 2010; Tsuda, Henry & Butler 2013). This tentative mechanism is valid only for the proximal alveolar generations, as it is believed that recirculation is absent in the most distal generations and air enters the alveolus with roughly radial direction (Kumar *et al.* 2009; Darquenne, Harrington & Prisk 2009).

4.3. *Surfactant drift through the alveolar opening*

The weakly nonlinear analysis of Bouchoris & Bontozoglou (2022) showed that, for soluble surfactants, surfactant flux Q_Γ has a steady streaming component, which results in an exit flux, $Q_{\Gamma 0}$, from the alveolar opening. This prediction is of particular interest in relation to techniques that probe exhaled air for micro-droplets originating from distal lung areas (Shmyrov *et al.* 2021). The accepted view is that these droplets form during re-opening of the small airways, after their closure during exhalation down to residual volume (Almstrand *et al.* 2010; Grotberg 2011). Airway lining fluid is known to contain surfactant molecules, whose analysis indicates that they most probably originate from the alveoli, where they are actually produced (Bernhard *et al.* 1997). Thus, the present prediction

https://doi.org/10.1017/jfm.2025.10798 Published online by Cambridge University Press

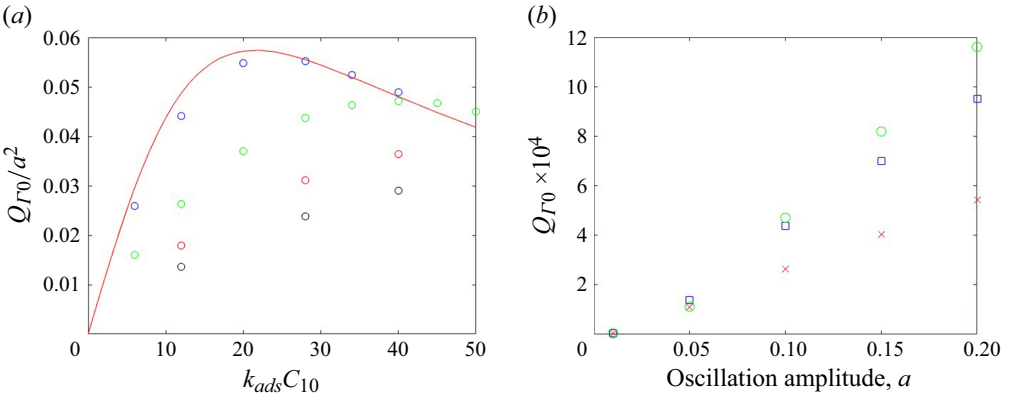


Figure 12. (*a*) The dependence of dimensionless surfactant drift on solubility, the former normalised with the square of the oscillation amplitude. Weakly nonlinear prediction (red line) and results for $a = 0.05$ (blue), 0.10 (green), 0.15 (red) and 0.20 (black circles). (*b*) The variation of dimensionless surfactant drift, $Q_{\Gamma 0}$, with amplitude for solubility $k_{ads}C_{10} = 12\ \mathrm{s}^{-1}$ (red crosses), $28\ \mathrm{s}^{-1}$ (blue squares) and $40\ \mathrm{s}^{-1}$ (green squares).

of a steady drift from the alveoli represents a potential mechanism for the transport of surfactant to the airways.

The dependence of the steady drift, $Q_{\Gamma 0}$, on surfactant solubility, $k_{ads}C_{10}$, is investigated in detail for a wide range of oscillation amplitudes in figure 12(*a*,*b*). The weakly nonlinear prediction $Q_{\Gamma 0}/a^2$ is plotted in figure 12(*a*) as a continuous red line and the drift is observed to increase from zero for the insoluble surfactant to a maximum of $Q_{\Gamma 0} \approx 0.0574\, a^2$ at $k_{ads}C_{10} = 22\ \mathrm{s}^{-1}$, and then slowly decrease for higher solubilities. The results for oscillations of finite amplitude indicate a gradual decrease in the coefficient of the $O(a^2)$ variation and a shift of the maximum to higher values. Thus, figure 12(*b*) (which is a mere re-plot of the data in figure 12*a*) shows that $Q_{\Gamma 0}$ increases roughly linearly with a. For the same amplitude, the increase with solubility is a consequence of the fact that the data are below the respective maximum for each amplitude, as depicted in figure 12(*a*).

5. Concluding remarks

An oscillating spherical cap, lined internally with a surfactant-laden liquid film, is considered a model of the dynamics of a single alveolus. The linear and weakly nonlinear analysis of this system around equilibrium by Bouchoris & Bontozoglou (2022) – in the lubrication limit of quasi-steady Stokes flow – is presently extended numerically to large-amplitude oscillations. The same boundary conditions are used at the rim, which enforce local conservation of the mass of water and surfactant without imposing any artificial constraint on the magnitude of the film thickness and surfactant concentration. In the case of a soluble surfactant, the adsorption to the liquid–air interface is described by Langmuir kinetics, modified by the inclusion of the intrinsic compressibility of the adsorbed monolayer. The parameters of the model of surfactant dynamics are best-fitted to achieve quantitative agreement with the behaviour of actual pulmonary surfactant preparations, as described in Appendix A.

The main qualitative difference from previous analysis, caused by large-amplitude oscillations, is the inclusion of phenomena related to monolayer collapse and replenishment. It is known (Krueger & Gaver 2000; Lee 2008; Parra & Perez-Gil 2015) that during strong compression of the interface, the surfactant monolayer reaches a limiting

https://doi.org/10.1017/jfm.2025.10798 Published online by Cambridge University Press

surface concentration, Γ_{max}, corresponding to minimum surface tension, $\sigma_{min} = \sigma(\Gamma_{max})$, and then collapses to form a sub-surface reservoir consisting of protrusions toward the interior that remain linked to the monolayer. This reservoir replenishes the monolayer during re-expansion of the interface and thus restricts the rise in surface tension.

The description of monolayer collapse and replenishment necessitates differentiating between the monolayer concentration, Γ_m, and the total surface concentration, Γ (with $\Gamma - \Gamma_m$ being the reservoir concentration), and independent conservation equations are now considered for Γ_m and for Γ. A key addition is the introduction of a novel kinetic expression to describe the 'two-way' exchange of surfactant between the monolayer and the reservoir. The kinetic expression contains a parameter that quantifies the stiffness of the monolayer, i.e. the approach to the maximum concentration needed to initiate collapse.

It is confirmed that the flow is driven by Marangoni stresses, developed as a result of differences in surfactant concentration between the rim and the interior of the alveolus. It is also found that the collapse of the monolayer does not hinder significantly the development of these stresses, unless the stiffness parameter becomes near singular. Thus, the first-order behaviour is similar for all oscillation amplitudes and a rough estimate of magnitude for the main flow variables can be provided from linear theory (see Appendix B below).

Capillary stresses, although dominated by Marangoni stresses on the interface, have a significant effect on internal variables such as the volumetric flow rate through the film and the shear stress along the epithelial wall. As capillary stresses are strongly modified during collapse because surface tension remains constant with further compression, the temporal variation of Q and τ_w deviates drastically from linear behaviour. Important second-order effects, such as the slow displacement of passive tracers on the interface and the drift of surfactant from the alveolus are investigated in detail and found to depend on both oscillation amplitude and surfactant solubility.

It is argued that some of the aforementioned results may tentatively be of physiological significance. The predicted nonlinear behaviour induces abrupt changes in wall shear stress, which vary both in magnitude and phase with oscillation amplitude. The overall effect, including the expected random variation of oscillation amplitude during consecutive breathing cycles, is equivalent to the imposition of near-random variability in the epithelial shear. As was demonstrated *in vitro* by Arold, Bartola & Suki (2009), stretching with random temporal variability, exerted on type-II alveolar cells, leads to enhanced surfactant secretion in comparison with purely periodic stretching. However, the rate of surfactant drift from the alveolus is presently predicted to increase with oscillation amplitude. Thus, the combination of the two effects appears to contribute to homeostasis at the alveolar level.

Also, the present prediction for the displacement of passive tracers by Marangoni stresses indicates that nano-particles deposited on the liquid layer may be cleared from the alveolus by the oscillation-induced flow field. The predicted exit half-time appears to agree with *in vivo* data, lending support to the argument that Marangoni flow provides a significant mechanism of alveolar clearance. However, the data did not involve direct measurement of alveolar retention, so other possibilities, such as uptake by alveolar macrophages and excretion involving the inflammatory system and lymphatics, cannot be excluded.

However, the passive tracer assumption is gradually invalidated with increasing particle diameter and two-way coupling between the particles and the flow will start to influence the dynamics. Such a dynamics would be more accurately described by interface-resolved simulations (Uhlmann 2008; Costa, Brandt & Picano 2020), which, however, are orders of magnitude more demanding in terms of computer resources and would also require a radical reformulation of the problem. Interface-resolved simulations would also allow

https://doi.org/10.1017/jfm.2025.10798 Published online by Cambridge University Press



Figure 13. A schematic indication of the change in interfacial surface area during recruiting of a contracted alveolus.

examination of the influence of the surfactant aggregates on the dynamics of the liquid film, an effect that has been currently neglected.

The present investigation is based on the assumed alveolar shape of a spherical cap in self-similar oscillation. Although this is the most frequently used model in the literature, both the true shape and the mode of oscillation of alveoli are subject to extensive discussion (Smaldone & Mitzner 2012; Sznitman 2022). On the one hand, space-filling constraints of the acinus promote polyhedral over spherical shapes. On the other hand, the self-similar oscillation, which corresponds to isotropic expansion i.e. alveolar surface area proportional to alveolar volume raised to the $2/3$ power, is but one of the possible modes of oscillation. There are other possibilities (Smaldone & Mitzner 2012), with most exotic one being alveolar recruitment, at least for part of the acinus. Recruitment assumes an accordion-like behaviour, with the alveolus collapsed during deep exhalation and reforming during inhalation. Thus, the alveolar volume changes while the epithelial surface area remains roughly constant.

Despite the above uncertainty in alveolar shape and oscillation pattern, it is believed that the conclusions of the present study are of more general validity, at least qualitatively. In particular, it is argued that periodic changes in interfacial surface area occur during the breathing manoeuvre for all the tentative expansion/contraction patterns, and a schematic demonstration for the 'accordion' model is shown in figure 13. Thus, gradients in surfactant concentration between the rim and the interior of the alveolus, which constitute the focus of the present study, remain in all cases the driving force for the shearing flow of the liquid layer that lines the alveolar epithelium.

Declaration of interests. The author reports no conflict of interest.

Appendix A.

The model of surfactant dynamics described in § 2.3 has been validated with data from Saad *et al.* (2010) and Xu *et al.* (2020). These authors measured the dynamic surface tension of a drop of pulmonary surfactant preparation, which experiences a periodic change in its surface area A. The drop rests on a flat circular substrate with sharp edges, so that its surface remains spherical, and the variations in surface area are caused by controlled rates of inflow and outflow of liquid from a hole at the centre of the substrate.

Under these conditions, surfactant concentrations, Γ and Γ_m, vary only with time, and the respective conservation equations simplify to the following expressions in terms of the known variables A and $\mathrm{d}A/\mathrm{d}t$:

$$\frac{\mathrm{d}\Gamma}{\mathrm{d}t}+\frac{\Gamma}{A}\frac{\mathrm{d}A}{\mathrm{d}t}+k_{ads}C_{10}\left[(\Gamma_{m,\infty}-\Gamma_m)-\frac{\Gamma_m}{K\,C_{10}}\right]=0, \tag{A1}$$

$$\frac{\mathrm{d}\Gamma_m}{\mathrm{d}t}+\frac{\Gamma_m}{A}\frac{\mathrm{d}A}{\mathrm{d}t}+k_{ads}C_{10}\left[(\Gamma_{m,\infty}-\Gamma_m)-\frac{\Gamma_m}{K\,C_{10}}\right] -k_r\left(\Gamma_{m,\infty}-\Gamma_m\right)(\Gamma-\Gamma_m)+\frac{k_{rc}}{(\Gamma_{max}-\Gamma_m)^2}=0. \tag{A2}$$

https://doi.org/10.1017/jfm.2025.10798 Published online by Cambridge University Press

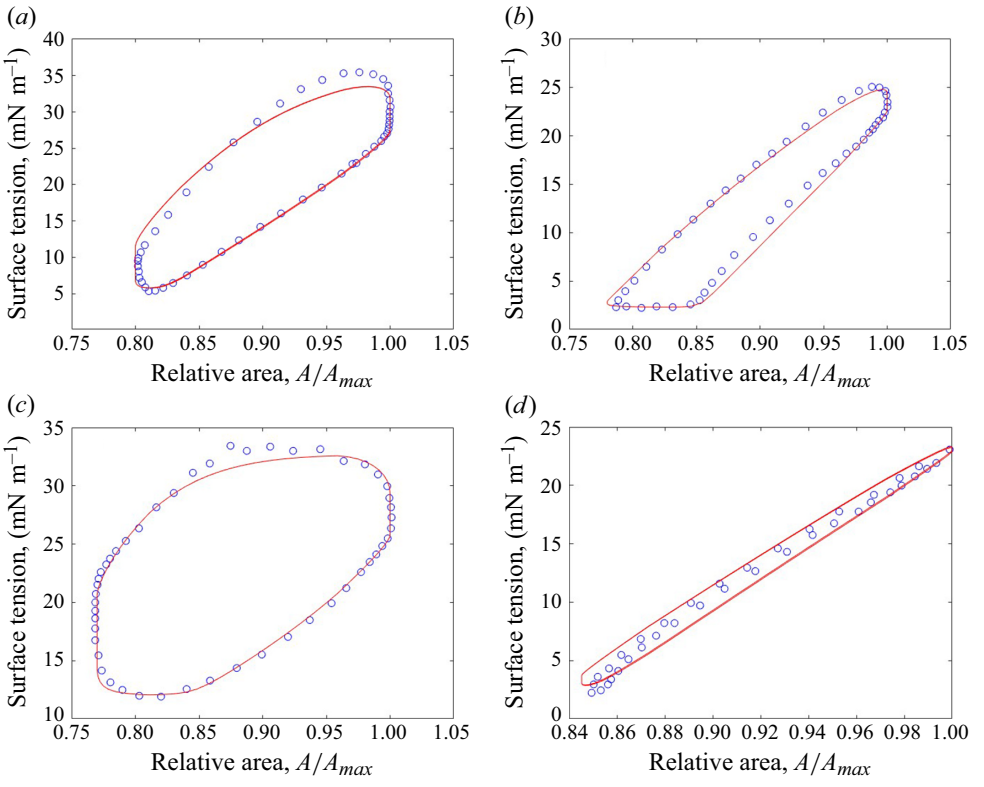


Figure 14. Predictions (red lines) and data (blue circles) by Saad *et al.* (2010) of the temporal variation of surface tension during periodic compression and expansion of the free surface of a droplet doped with surfactant. Panels (*a*) and (*c*) are for soluble surfactant with $k_{ads}C_{10} = 12\,\mathrm{s}^{-1}$ and $28\,\mathrm{s}^{-1}$, respectively. Panels (*b*) and (*d*) are for an insoluble surfactant $k_{ads}C_{10} = 0\,\mathrm{s}^{-1}$ and differ only in the extent of collapse.

Equations (A1)–(A2) are integrated with a Newton–Raphson iterative scheme, using implicit Euler differencing for the derivatives.

The key parameters of the surfactant, KC_{10}, $k_{ads}C_{10}$, α, k_r and k_{rc}, are fitted, so that predictions by the above model agree quantitatively with the data. Comparisons are shown in figure 14(*a–d*) and the best-fit values are physically meaningful and in the expected range (Bouchoris & Bontozoglou 2021). It is noted that some of these values differ from the ones reported by Bouchoris & Bontozoglou (2021), because an improved model is presently used to describe monolayer collapse during deep compression and replenishment during re-expansion.

Appendix B.

In this appendix are examined in detail the gross characteristics of the main flow variables, $h(x,t)$, $u_s(x,t)$, $Q(x,t)$ and $\tau_w(x,t)$, as the oscillation amplitude increases. The goal is to test the accuracy with which they may be roughly estimated from the linear solution.

First, the displacement of the interface from its equilibrium position is considered, as quantified by its extreme values $h_{min}(x) - H(x)$ and $h_{max}(x) - H(x)$. These extrema are normalised with the local equilibrium value, forming the ratios $\Delta h_{min} = [h_{min}(x) - H(x)]/H(x)$ and $\Delta h_{max} = [h_{max}(x) - H(x)]/H(x)$. The normalisation is motivated by the previous finding (Bouchoris & Bontozoglou 2022) of a trivial solution (of the

https://doi.org/10.1017/jfm.2025.10798 Published online by Cambridge University Press

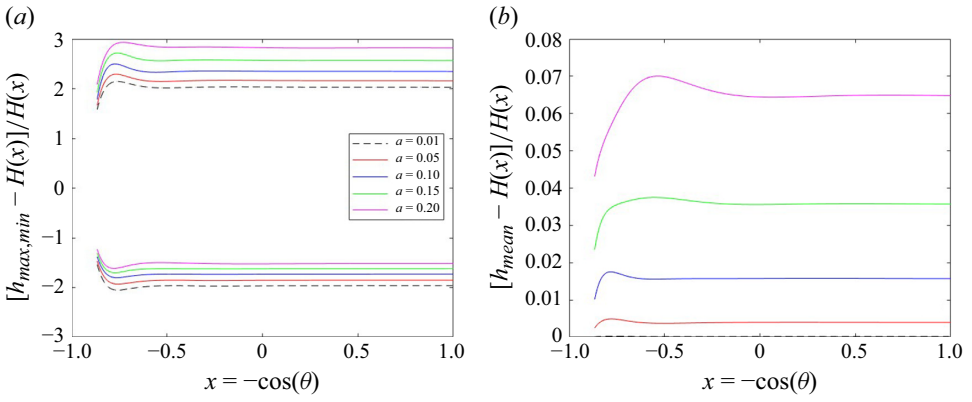


Figure 15. (*a*) The maximum and minimum interface displacement normalised with the equilibrium film thickness and the oscillation amplitude. (*b*) The mean liquid film thickness normalised with the equilibrium thickness. Oscillation amplitudes $a = 0.01$ (dashed black), $a = 0.05$ (red), $a = 0.10$ (blue), $a = 0.15$ (green) and $a = 0.20$ (magenta).

equations but not the boundary conditions) with purely radial velocities and displacement proportional to the equilibrium film thickness. Thus, the deviations of Δh_{min} and Δh_{max} from uniform values along the entire interface are indicative of the intensity of local shearing motion.

In the linear limit, Δh_{min} and Δh_{max} are proportional to the alveolar oscillation amplitude. Thus, the ratios $\Delta h_{min}/a$ and $\Delta h_{max}/a$, plotted for $a = 0.01,\ 0.05,\ 0.10,\ 0.15$ and 0.20 in figure 15(*a*), offer a first view of the deviations from linearity. It is readily observed that $\Delta h_{min}/a$ and $\Delta h_{max}/a$ vary strongly in the region from the rim and up to $x \approx -0.5$ ($\theta = 60°$), while they attain relatively uniform values deeper in the interior of the alveolus. This trend indicates that the shearing motion is more intense in the first 30° from the alveolar entrance.

In addition, it is observed from figure 15(*a*) that the symmetry around the equilibrium position (which holds for $a = 0.01$) is gradually broken, with the liquid film thickening more during alveolar contraction and thinning less during expansion. This is further confirmed by figure 15(*b*), which displays the term $\Delta\bar{h}(x) = [\bar{h}(x) - H(x)]/H(x)$, with $\bar{h}(x)$ the mean film thickness at location x. The increase in the mean film thickness is non-uniform close to the entrance, with the affected region increasing significantly with oscillation amplitude. The generally observed displacement of the liquid film thickness towards positive values is a purely geometrical effect because the variation in the interfacial surface area is not symmetric around its equilibrium value when the radius oscillates with finite amplitude.

Next, we examine the order of magnitude of the surface velocity, $u_s(x, t)$, volumetric flow rate, $Q(x, t)$ and wall shear stress, $\tau_w(x, t)$. Figure 16(*a*,*b*,*c*) shows the maximum and minimum values attained by the above variables during an oscillation cycle, normalised with the oscillation amplitude. The amplitudes considered cover a wide range, starting from the linear limit, $a = 0.01$, and going up to $a = 0.20$, where extensive monolayer collapse occurs. It is observed that the results for the surface velocity are almost perfectly superimposed, indicating that the Marangoni stresses totally dominate the interfacial dynamics for all oscillation amplitudes. In contrast, the volumetric flow rate and the wall shear stress are also affected by capillary stresses and viscosity. (The effect of capillarity is clearly witnessed by the oscillatory variation of $Q_{max},\ Q_{min}$ with x.) However, it is evident that the variations of $Q_{max}/a,\ Q_{min}/a$ and $\tau_{w,max}/a,\ \tau_{w,min}/a$ with amplitude

https://doi.org/10.1017/jfm.2025.10798 Published online by Cambridge University Press

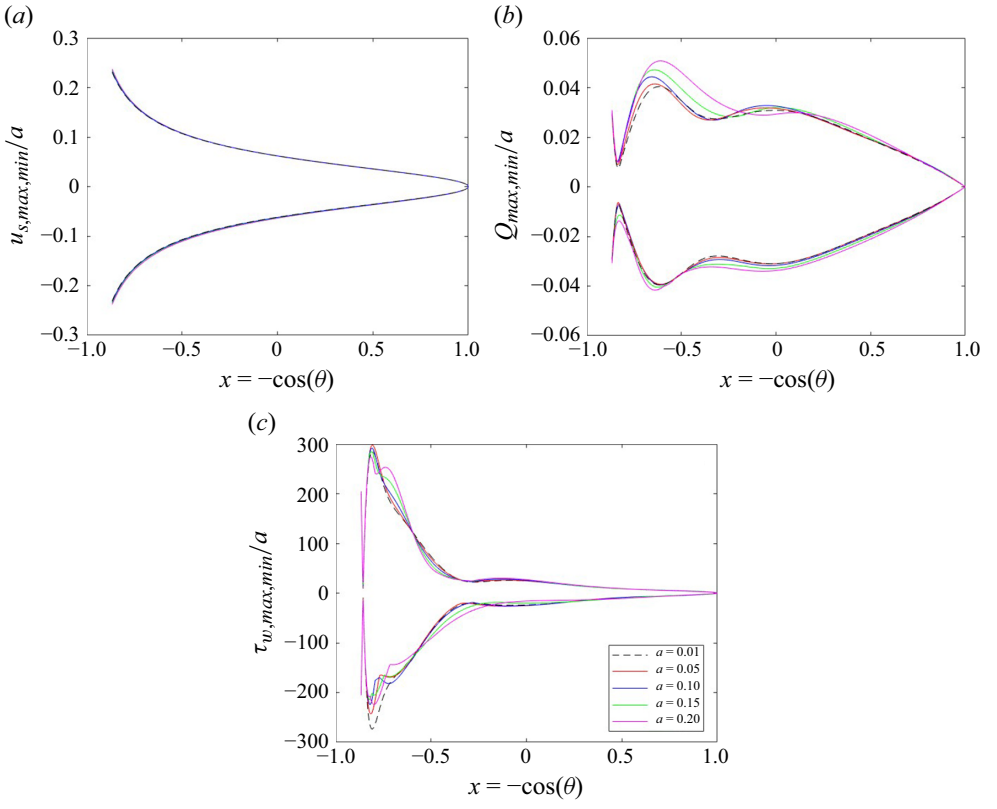


Figure 16. The maxima and minima of (*a*) surface velocity, (*b*) volumetric flow rate and (*c*) wall shear stress along the film for oscillation amplitudes $a = 0.01$ (dashed black), $a = 0.05$ (red), $a = 0.10$ (blue), $a = 0.15$ (green) and $a = 0.20$ (magenta).

are not dramatic, indicating that the role of oscillation amplitude is described by a regular expansion, i.e. higher-order terms provide small corrections. Thus, it appears that a convenient rule of thumb for rough estimates of magnitude is to use the linear results with any value of the amplitude a.

References

Almstrand, A.-C., Bake, B., Ljungström, E., Larsson, P., Bredberg, A., Mirgorodskaya, E. & Olin, A.-C. 2010 Effect of airway opening on production of exhaled particles. *J. Appl. Physiol.* **108**, 584–588.

Arold, S.P., Bartolák-Suki, E., Suki, B. 2009 Variable stretch pattern enhances surfactant secretion in alveolar type ii cells in culture. *Am. J. Physiol. Lung Cell. Mol. Physiol.* **296**, L574–L581.

Bailey, M.R., Frances, A.F. & James, A.C. 1982 *The long-term clearance kinetics of insoluble particles from the human lung*. Pergamon.

Bailey, M.R., Fry, F.A. & James, A.C. 1985 Long-term retention of particles in the human respiratory tract. *J. Aerosol Sci.* **16** (4), 295–305.

Baoukina, S., Monticelli, L., Risselada, H.J., Marrink, S.J. & Tieleman, D.P. 2008 The molecular mechanism of lipid monolayer collapse. *Proc. Natl Acad. Sci. USA* **105** (31), 10803–10808.

Baoukina, S. & Tieleman, D.P. 2011 Lung surfactant protein SP-B promotes formation of bilayer reservoirs from monolayer and lipid transfer between the interface and subphase. *Biophys. J.* **100**, 1678–1687.

Bastacky, J., Lee, C.Y., Goerke, J., Koushafar, H., Yager, D., Kenaga, L., Speed, T.P., Chen, Y. & Clements, J.A. 1995 Alveolar lining layer is thin and continuous: low-temperature scanning electron microscopy of rat lung. *J. Appl. Physiol.* **79**, 1615–1628.

https://doi.org/10.1017/jfm.2025.10798 Published online by Cambridge University Press

BERNHARD, W., HAAGSMAN, H.P., TSCHERNIG, T., POETS, C.F., POSTLE, A.D., VAN EIJK, M.E. & VON DER HARDT, H. 1997 Conductive airway surfactant: surface-tension function, biochemical composition, and possible alveolar origin. *Am. J. Respir. Cell Mol. Biol.* **17**, 41–50.

BLYTH, M.G. & POZRIKIDIS, C. 2004 Effect of surfactant on the stability of film flow down an inclined plane. *J. Fluid Mech.* **521**, 241–250.

BOUCHORIS, K. & BONTOZOGLOU, V. 2021 A model of lung surfactant dynamics based on intrinsic interfacial compressibility. *Colloids Surf. A: Physicochem. Engng Aspects* **624**, 126839.

BOUCHORIS, K. & BONTOZOGLOU, V. 2022 Surfactant-laden film lining an oscillating cap: problem formulation and weakly nonlinear analysis. *J. Fluid Mech.* **944**, A501–37.

BYKOV, A.G., MILYAEVA, O.Y., ISAKOV, N.A., MICHAILOV, A.V., LOGLIO, G., MILLER, R. & NOSKOV, B.A. 2021 Dynamic properties of adsorption layers of pulmonary surfactants. Influence of matter exchange with bulk phase. *Colloids Surf. A Physicochem. Engng Aspects* **611**, 125851.

CONSTANTE-AMORES, C.R., BATCHVAROV, A., KAHOUADJI, L., SHIN, S., CHERGUI, J., JURIC, D. & MATAR, O.K. 2021 Role of surfactant-induced Marangoni stresses in drop-interface coalescence. *J. Fluid Mech.* **925**, A15.

COSTA, P., BRANDT, L. & PICANO, F. 2020 Interface-resolved simulations of small inertial particles in turbulent channel flow. *J. Fluid Mech.* **883**, A54.

CRANE, J.M., PUTZ, G. & HALL, S.B. 1999 Persistence of phase coexistence in disaturated phosphatidylcholine monolayers at high surface pressures. *Biophys. J.* **77**, 3134–3143.

CRASTER, R.V. & MATAR, O.K. 2009 Dynamics and stability of thin liquid films. *Rev. Modern Phys.* **81**, 1131–1198.

D'ALESSIO, S.J.D. & PASCAL, J.P. 2021 Long-wave instability in thin heated films doped with soluble surfactants. *Intl J. Non-Linear Mech.* **136**, 103784.

DARQUENNE, C., HARRINGTON, L. & PRISK, G.K. 2009 Alveolar duct expansion greatly enhances aerosol deposition: a three-dimensional computational fluid dynamics study. *Phil. Trans. R. Soc. A* **367** (1896), 2333–2346.

ESPINOSA, F.F. & KAMM, R.D. 1997 Thin layer flows due to surface tension gradients over a membrane undergoing nonuniform periodic strain. *Ann. Biomed. Engng* **25**, 913–925.

FAINERMAN, V.B., MILLER, R. & KOVALCHUK, V.I. 2002 Influence of the compressibility of adsorbed layers on the surface dilational elasticity. *Langmuir* **18**, 7748–7752.

FERIN, J. 1994 Pulmonary retention and clearance of particles. *Toxicol. Lett.* **72** (1–3), 121–125.

FILOCHE, M., TAI, C.-F. & GROTBERG, J.B. 2015 Three-dimensional model of surfactant replacement therapy. *Proc. Natl Acad. Sci. USA* **112**, 9287–9292.

FRENKEL, A.L. & HALPERN, D. 2002 Stokes-flow instability due to interfacial surfactant. *Phys. Fluids* **14**, L45–L48.

GAVER, D.P. & GROTBERG, J.B. 1990 The dynamics of a localized surfactant on a thin film. *J. Fluid Mech.* **213**, 127–148.

GRADON, L. & PODGORSKI, A. 1989 Hydrodynamical model of pulmonary clearance. *Chem. Engng Sci.* **44**, 741–749.

GROTBERG, J.B. 2011 Respiratory fluid mechanics. *Phys. Fluids* **23**, 021301.

HABER, S., BUTLER, J.P., BRENNER, H., EMMANUEL, I. & TSUDA, A. 2000 Shear flow over a self-similar expanding pulmonary alveolus during rhythmical breathing. *J. Fluid Mech.* **405**, 243–268.

HALPERN, D., FUJIOKA, H., TAKAYAMA, S. & GROTBERG, J.B. 2008 Liquid and surfactant delivery in the pulmonary airways. *Resp. Physiol. Neurobiol.* **163**, 222–231.

HALPERN, D., JENSEN, O.E. & GROTBERG, JB. 1998 A theoretical study of surfactant and liquid delivery into the lung. *J. Appl. Physiol.* **85**, 333–352.

HENRY, S. & TSUDA, A.F. 2010 Flow and particle tracks in model acini. *ASME J. Biomech. Engng* **132**, 101001.

HU, T., FU, Q. & YANG, L. 2020 Falling film with insoluble surfactants: effects of surface elasticity and surface viscosities. *J. Fluid Mech.* **873**, 18–48.

INGENITO, E.P., MARK, L., MORRIS, J., ESPINOSA, F.F., KAMM, R.D. & JOHNSON, M. 1999 Biophysical characterization and modeling of lung surfactant components. *J. Appl. Physiol.* **86** (5), 1702–1714.

KALOGIROU, A. & PAPAGEORGIOU, D.T. 2015 Nonlinear dynamics of surfactant-laden two-fluid Couette flows in the presence of inertia. *J. Fluid Mech.* **802**, 5–36.

KANG, D., CHUGUNOVA, M., NADIM, A., WARING, A.J. & WALTHER, F.J. 2018 Modeling coating flow and surfactant dynamics inside the alveolar compartment. *J. Engng Maths* **113**, 23–43.

KILBURN, K.H. 1968 A hypothesis for pulmonary clearance and its implications. *Am. Rev. Resp. Disease* **98** (3), 449–463.

https://doi.org/10.1017/jfm.2025.10798 Published online by Cambridge University Press

KIM, K., CHOI, S.Q., ZASADZINSKI, J.A. & SQUIRES, T.M. 2011 Interfacial microrheology of dppc monolayers at the air–water interface. *Soft Matter* **7**, 7782–7789.

KOLANJIYIL, A.V. & KLEINSTREUER, C. 2019 Modeling airflow and particle deposition in a human acinar region. *Comput. Math. Methods Med.* **2019**, 5952941.

KOVALCHUK, V.I., LOGLIO, G., FAINERMAN, V.B. & MILLER, R. 2004 Interpretation of surface dilational elasticity data based on an intrinsic two-dimensional interfacial compressibility model. *J. Colloid Interface Sci.* **270**, 475–482.

KOVALCHUK, V.I., MILLER, R., FAINERMAN, V.B. & LOGLIO, G. 2005 Dilational rheology of adsorbed surfactant layers - role of the intrinsic two-dimensional compressibility. *Adv. Colloid Interface Sci.* **114–115**, 303–312.

KRUEGER, M.A. & GAVER, D.P. 2000 A theoretical model of pulmonary surfactant multilayer collapse under oscillating area conditions. *J. Colloid Interface Sci.* **229**, 353–364.

KUMAR, H., TAWHAI, M.H., HOFFMAN, E.A. & LIN, C.L. 2009 The effects of geometry on airflow in the acinar region of the human lung. *J. Biomech.* **42**, 1635–1642.

LEE, K.Y.C. 2008 Collapse mechanisms of langmuir monolayers. *Annu. Rev. Phys. Chem.* **59**, 771–791.

LIPP, M.M., LEE, K.Y.C., TAKAMOTO, D.Y., ZASADZINSKI, J.A. & WARING, A.J. 1998 Coexistence of buckled and flat monolayers. *Phys. Rev. Lett.* **81** (8), 1650–1653.

LIPPMANN, M., YEATES, D.B. & ALBERT, R.E. 1980 Deposition, retention, and clearance of inhaled particles. *Occup. Environ. Med.* **37** (4), 337–362.

LIVANOS, A., BOUCHORIS, K., ASLANI, K.E., GOURGOULIANIS, K. & BONTOZOGLOU, V. 2024 Prediction of shear stress imposed on alveolar epithelium of healthy and diseased lungs. *Biomech. Model. Mechanobiol.* **23** (6), 2213–2227.

MANIKANTAN, H. & SQUIRES, T.M. 2020 Surfactant dynamics: hidden variables controlling fluid flows. *J. Fluid Mech.* **892**, P11–115.

MARSH, D. & KING, M.D. 1986 Prediction of the critical micelle concentrations of mono- and di-acyl phospholipids. *Chem. Phys. Lipids* **42**, 271–277.

MATAR, O., ZHANG, Y.L. & CRASTER, R.V. 2003 Surfactant driven flows overlying a hydrophobic epithelium: film rupture in the presence of slip. *J. Colloid Interface Sci.* **264**, 160–175.

MIGUET, J., DORBOLO, S. & SCHEID, B. 2024 Antibubble column: a mean to measure and enhance liquid–gas mass transfer through surfactant-laden interfaces. *Chem. Engng J.* **498**, 153276.

MURADOGLU, M., ROMANÒ, F., FUJIOKA, H. & GROTBERG, J.B. 2019 Effects of surfactant on propagation and rupture of a liquid plug in a tube. *J. Fluid Mech.* **872**, 407–437.

OBERDOERSTER, G. 1988 Lung clearance of inhaled insoluble and soluble particles. *J. Aerosol Med.* **1** (4), 289–330.

OCHS, M., NYENGAARD, J.R., JUNG, A., KNUDSEN, L., VOIGT, M., WAHLERS, T., RICHTER, J. & GUNDERSEN, H. 2004 The number of alveoli in the human lung. *Am. J. Respir. Crit. Care Med.* **169**, 120–124.

ORON, A., DAVIS, S.H. & BANKOFF, G.S. 1997 Long-scale evolution of thin liquid films. *Rev. Mod. Phys.* **69**, 931–980.

PARRA, E. & PEREZ-GIL, J. 2015 Composition, structure and mechanical properties define performance of pulmonary surfactant membranes and films. *Chem. Phys. Lipids* **185**, 153–175.

PEREIRA, A., TREVELYAN, P.M.J., THIELE, U. & KALLIADASIS, S. 2007 Dynamics of a horizontal thin liquid film in the presence of reactive surfactants. *Phys. Fluids* **19**, 112102.

PEREZ-GIL, J. 2008 Structures of pulmonary surfactant membranes and films: the role of proteins and lipid-proteins interactions. *Biochim. Biophys. Acta* **1778**, 1676–1695.

PHAN, M.D., LEE, J. & SHIN, K. 2016 Collapsed states of langmuir monolayers. *J. Oleo Sci.* **65**, 385–397.

PODGORSKI, A. & GRADON, L. 1993 An improved mathematical model of hydrodynamical self-cleansing of pulmonary alveoli. *Ann. Occup. Hyg.* **37**, 347–365.

POSSMAYER, F., NAG, K., RODRIGUEZ, K., QANBAR, R. & SCHÜRCH, S. 2001 Surface activity in vitro: role of surfactant proteins. *Compar. Biochem. Physiol. A* **129**, 209–220.

ROMANÒ, F., MURADOGLU, M. & GROTBERG, J.B. 2022 Effect of surfactant in an airway closure model. *Phys. Rev. Fluids* **7** (9), 093103.

RUGONYI, S., BISWAS, S.C. & HALL, S.B. 2008 The biophysical function of pulmonary surfactant. *Resp. Physiol. Neurobiol.* **163**, 244–255.

SAAD, S.M.I., NEUMANN, A.W. & ACOSTA, E.J. 2010 A dynamic compression-relaxation model for lung surfactants. *Colloids Surf. A Physicochem. Engng Aspects* **354**, 34–44.

SAMANTA, A. 2021 Effect of surfactant on the linear stability of a shear-imposed fluid flowing down a compliant substrate. *J. Fluid Mech.* **920**, A23.

https://doi.org/10.1017/jfm.2025.10798 Published online by Cambridge University Press

SAMANTA, A. 2025 Role of soluble surfactant in linear stability of a liquid film flowing down a compliant substrate. *J. Fluid Mech.* **1011**, A6.

SCHIEF, W.R., ANTIA, M., DISCHER, B.M., HALL, S.B. & VOGEL, V. 2003 Liquid–crystalline collapse of pulmonary surfactant monolayers. *Biophys. J.* **84** (6), 3792–3806.

SCHÜRCH, A., GREEN, F.H.Y. & BACHOFEN, H. 1998 Formation and structure of surface films: captive bubble surfactometry. *Biochim. Biophys. Acta* **1408**, 180–202.

SHMYROV, A., MIZEV, A., MIZEVA, I. & SHMYROVA, A. 2021 Electrostatic precipitation of exhaled particles for tensiometric examination of pulmonary surfactant. *J. Aerosol Sci.* **151**, 105622.

SMALDONE, G.C. & MITZNER, W. 2012 Viewpoint: unresolved mysteries. *J. Appl. Physiol.* **113**, 1945–1947.

SMITH, D.J., EAMONN, AG. & BLAKE, J.R. 2008 Modelling mucociliary clearance. *Respir. Physiol. Neurobiol.* **163**, 178–188.

STAROV, V. & IVANOV, I. 2004 *Fluid Mechanics of Surfactant and Polymer Solutions*. Springer-Verlag Wien GmbH.

SZNITMAN, J. 2022 Revisiting airflow and aerosol transport phenomena in the deep lungs with microfluidics. *Chem. Rev.* **122**, 7182–7204.

TSUDA, A.F., HENRY, S. & BUTLER, J.P. 2008 Gas and aerosol mixing in the acinus. *Respir. Physiol. Neurobiol.* **163**, 139–149.

TSUDA, A.F., HENRY, S. & BUTLER, J.P. 2013 Particle transport and deposition: basic physics of particle kinetics. *Compr. Physiol.* **3**, 1437–1471.

UHLMANN, M. 2008 Interface-resolved direct numerical simulation of vertical particulate channel flow in the turbulent regime. *Phys. Fluids* **20**, 053305.

WEI, H.-H., BENINTENDI, S.W., HALPERN, D. & GROTBERG, J.B. 2003 Cycle-induced flow and transport in a model of alveolar liquid lining. *J. Fluid Mech.* **483**, 1–36.

WEI, H.-H., FUJIOKA, H., HIRSCHL, R.B. & GROTBERG, J.B. 2005 A model of flow and surfactant transport in an oscillatory alveolus partially filled with liquid. *Phys. Fluids* **17**, 031510.

WÜSTNECK, N., WÜSTNECK, R., FAINERMAN, V.B., MILLER, R. & PISON, U. 2001 Interfacial behaviour and mechanical properties of spread lung surfactant protein/lipid layers. *Colloids Surf. B: Biointerfaces* **21**, 191–205.

WÜSTNECK, R., PEREZ-GIL, J., WÜSTNECK, N., CRUZ, A., FAINERMAN, V.B. & PISON, U. 2005 Interfacial properties of pulmonary surfactant layers. *Adv. Colloid Interface Sci.* **117**, 33–58.

WÜSTNECK, R., PEREZ-GIL, J., WÜSTNECK, N., CRUZ, A., FAINERMAN, V. & PISON, U. 2005 Interfacial properties of pulmonary surfactant layers. *Adv. Colloid Interface Sci.* **117**, 33–58.

XU, L., YANG, Y. & ZUO, Y.Y. 2020 Atomic force microscopy imaging of adsorbed pulmonary surfactant films. *Biophys. J.* **119**, 756–766.

YAN, W., PIKNOVA, B. & HALL, S.B. 2005 The collapse of monolayers containing pulmonary surfactant phospholipids is kinetically determined. *Biophys. J.* **89**, 306–314.

ZASADZINSKI, J.A., DING, J., WARRINER, H.E., BRINGEZU, F. & WARING, A.J. 2001 The physics and physiology of lung surfactants. *Curr. Opinion Colloid Interface Sci.* **6**, 506–513.

ZELIG, D. & HABER, S. 2002 Hydrodynamic cleansing of pulmonary alveoli. *SIAM J. Appl. Maths* **63**, 195–221.

ZELTNER, T.B., SWEENEY, T.D., SKORNIK, W.A., FELDMAN, H.A. & BRAIN, J.D. 1991 Retention and clearance of 0.90-micron particles inhaled by hamsters during rest or exercise. *J. Appl. Physiol.* **70**, 1137–1145.

ZHANG, H., WANG, Y.E., FAN, Q. & ZUO, Y.Y. 2011 On the low surface tension of lung surfactant. *Langmuir* **27**, 8351–8358.

ZUO, Y.Y., GITIAFROZ, R., ACOSTA, E., POLICOVA, Z., COX, P.N., HAIR, M.L. & NEUMANN, A.W. 2005 Effect of humidity on the adsorption kinetics of lung surfactant at air-water interfaces. *Langmuir* **21** (23), 10593–10601.

ZUO, Y.Y., RIMEI, C., XIANJU, W., JINLONG, Y., POLICOVA, Z. & NEUMANN, A.W. 2016 Phase transitions in dipalmitoylphosphatidylcholine monolayers. *Langmuir* **32** (33), 8501–8506.

ZUO, Y.Y., VELDHUIZEN, R., NEUMANN, A.W., PETERSEN, N.O. & POSSMAYER, F. 2008 Current perspectives in pulmonary surfactant–inhibition, enhancement and evaluation. *Biochim. Biophys. Acta* **1778**, 1947–1977.

https://doi.org/10.1017/jfm.2025.10798 Published online by Cambridge University Press